

BIROn - Birkbeck Institutional Research Online

Nottingham, M. and Stuart, F. and Chen, B. and Zurakowska, M. and Gilmour, J. and Alexander, L. and Crawford, Ian and Joy, K. (2022) Complex burial histories of Apollo 12 basaltic soil grains derived from cosmogenic noble gases: implications for local regolith evolution and future in situ investigations. *Meteoritics and Planetary Science* 57 (3), pp. 603-634. ISSN 1086-9379.

Downloaded from: <https://eprints.bbk.ac.uk/id/eprint/47741/>






Usage Guidelines:

Please refer to usage guidelines at <https://eprints.bbk.ac.uk/policies.html>

or alternatively

contact lib-eprints@bbk.ac.uk.

Complex burial histories of Apollo 12 basaltic soil grains derived from cosmogenic noble gases: Implications for local regolith evolution and future in situ investigations

Mark C. NOTTINGHAM ^{*1,2,3}, Finlay M. STUART ⁴, Biying CHEN⁴, Marta ZURAKOWSKA⁴,
Jamie D. GILMOUR ³, Louise ALEXANDER^{1,2}, Ian A. CRAWFORD ^{1,2}, and
Katherine H. JOY ³

¹Department of Earth and Planetary Science, Birkbeck College, University of London, Malet Street, London WC1E 7HX, UK

²The Centre for Planetary Sciences at UCL-Birkbeck, Gower Street, London WC1E 6BT, UK

³Department of Earth and Environmental Sciences, The University of Manchester, Oxford Road, Manchester M13 9PL, UK

⁴Isotope Geosciences Unit, Scottish Universities Environmental Research Centre (SUERC), East Kilbride G75 0QF, UK

*Corresponding author. E-mail: mark.nottingham@manchester.ac.uk

(Received 17 November 2020; revision accepted 16 December 2021)

Abstract—We report the concentrations and isotope ratios of light noble gases (He, Ne, Ar) in 10 small basalt fragments derived from lunar regolith soils at the Apollo 12 landing site. We use cosmic ray exposure (CRE) and shielding condition histories to consider their geological context. We have devised a method of using cosmogenic Ne isotopes to partition the CRE history of each sample into two stages: a duration of “deep” burial (shielding of 5–500 g cm⁻²) and a duration of near-surface exposure (shielding of 0 g cm⁻²). Three samples show evidence of measurable exposure at the lunar surface (durations of between 6 ± 2 and 7 ± 2 Myr). The remaining seven samples show evidence of a surface residence duration of less than a few hundred thousand years prior to collection. One sample records a single-stage CRE age range of between 516 ± 36 and 1139 ± 121 Myr, within 0–5 g cm⁻² of the lunar surface. This is consistent with derivation from ballistic sedimentation (i.e., local regolith reworking) during the Copernicus crater formation impact at ~800 Myr. The remaining samples show CRE age clusters around 124 ± 11 Myr and 188 ± 15 Myr. We infer that local impacts, including Surveyor crater (180–240 Ma) and Head crater (144 Ma), may have brought these samples to depths where the cosmic ray flux was intense enough to produce measurable cosmogenic Ne isotopes. More recent small impacts that formed unnamed craters may have exhumed these samples from their deep shielding conditions to the surface (i.e., ~0–5 g cm⁻²) prior to collection from the lunar surface during the Apollo 12 mission.

INTRODUCTION

Astronomical phenomena, including solar activity and galactic cosmic rays (GCRs), may have played a significant role in solar system history, possibly including the development of life on Earth (e.g., Airapetian et al., 2016; Atri & Melott, 2014; Cohen et al., 2012; Erlykin & Wolfendale, 2010; Globus & Blandford, 2020; Rodgers-Lee et al., 2020; Todd, 1994). The Earth’s record of the ancient cosmic radiation environment has largely been erased by weathering and geological processes. The Moon has never been affected

by plate tectonics or processing by a hydrosphere or biosphere, so the record of these astronomical phenomena may be better preserved in lunar rocks than on Earth (Crawford et al., 2010, 2021; Fagents et al., 2010; McKay et al., 1991; Spudis, 1996). Moreover, much of the low-energy space radiation flux (e.g., solar wind and solar cosmic ray [SCR] flux) does not reach the Earth’s surface, so investigation via the analysis of terrestrial geological samples is not possible. In contrast, the Moon lacks an atmosphere and currently has no appreciable magnetic field (Mighani et al., 2020), so much of the lunar surface experiences direct exposure to

the prevailing high- and low-energy space radiation environment (Omidi et al., 2019). It has, thus, been hypothesized that the regolith cover of the Moon's surface preserves a record of astronomical phenomena from more than 4 billion years of solar system history (e.g., Crawford et al., 2007, 2021; McKay et al., 1991; Spudis, 1996). This record has the potential to act as a proxy for the space exposure of the whole Earth–Moon system through time (Crawford et al., 2007). However, to interpret this astronomical record, it is first necessary to understand the evolution of the lunar regolith.

Our understanding of the geological history of the Moon is largely inferred from the detailed investigations of a select number of specific sites on the lunar surface. These are sites for which we have access to returned lunar samples that can be used in Earth-based laboratory analyses (e.g., the Apollo 12 landing site; see the Apollo 12 Landing Site, Previous Studies and Current Geological Perspectives section). The history of the regolith at any given locality is complex, and understanding of this history is necessary if we are to discern how findings relate to astronomical phenomena the Moon has experienced. Here, we show that noble gases extracted from individual regolith particles can provide more detailed insights into this localized regolith evolution (see also Wieler, 2016).

To achieve this, we have developed a novel method for calculating the isotopic composition (and fraction concentrations) of noble gas endmember components, and explore the potential to use this method to establish two-stage cosmic ray exposure (CRE) histories for a suite of basalt fragments derived from Apollo 12 soil samples. This study builds upon the previous petrological characterization of 10 basalt fragments (derived from Apollo 12 soils 12003 and 12030) and three fragments of a reference crystalline rock (derived from hand specimen sample 12022) by Alexander et al. (2014) and Snape et al. (2014). Our work forms a part of a broader investigation, exploring the potential for using small basalt fragments derived from lunar soil samples to aid our understanding of lunar regolith evolution and the Moon's interaction with the space environment (i.e., galactic history, solar history, delivery of meteoritic material) through time (Crawford et al., 2021; Joy et al., 2016; McKay et al., 1991; Spudis, 1996). In addition, most lunar basalt rocks date from a significant period of lunar geological history (i.e., the infilling of mare regions). The ability to discern individual basalt flows from the Apollo 12 region and investigate their burial history can directly inform our understanding of the impacts that have distributed this material across the lunar surface. Furthermore, the study of these rock types and their potential source

craters can partially inform our understanding of the thickness of these basalt flows.

In this study, we used the concentrations and isotopic signatures of He, Ne, and Ar, which represent an amalgamation of solar wind implantation and cosmic ray triggered nuclear reactions (e.g., cosmogenic spallation), to constrain the CRE histories of individual Apollo basaltic fragments and the evolution of the Apollo 12 landing site. We categorized these isotopic signatures broadly into two endmembers: “trapped endmembers” (mixtures of implanted solar wind and other minor components) and sample-specific “cosmogenic endmembers” (formed via nuclear reactions between exogenous high-energy radiation associated with the SCR and GCR fluxes and target elements within lunar rocks). We then sought to partition the CRE histories of these samples into two stages of exposure, using the measured Ne isotopic compositions. One is defined as occurring at the lunar surface (where the production rates of cosmogenic nuclides are higher due to SCR spallation interactions) and one at depth (where production rates and $^{21}\text{Ne}/^{22}\text{Ne}$ ratios increase), where the depth is calculated based on constraints indicated by the measured data. This approach differs from previous studies that have investigated two-stage CRE models, such as the study by Burnett et al. (1975) and Eugster et al. (1984). These studies applied additional assumptions to their noble gas data (e.g., during gas fraction partitioning) or include multiple isotopic systems in their construction of their two-stage CRE models. In contrast, our method allows a two-stage CRE history to be established using a single-element exposure age system, and commonly used analytical protocols.

Some terms used in this study are inconsistent in their definition throughout literature sources. We, therefore, define the meaning we apply to the following terms. (1) CRE (age)—the (duration of) irradiation by cosmic rays for a given sample (irrespective of shielding conditions; we note the difference between lunar and terrestrial applications of this term); (2) “trapped component”—any gases adsorbed, or implanted, into the rock sample.

We discuss burial depths in terms of radiation lengths or interaction depths (g cm^{-2}). This allows us to discuss differences in shielding in their entirety (i.e., those caused by sample size change driven by processes such as comminution of larger samples, as well as changes in burial depth). The methods applied in this study do not allow us to discern among the various mechanisms that lead to shielding depth changes (e.g., surface erosion: Arvidson et al. [1975] and Basilevsky et al. [2013]; regolith gardening: Costello et al., 2018; and mass wasting processes: Bickel et al., 2020).

Noble Gas Reservoirs and Interactions with the Lunar Surface

Noble gases are extensively used in lunar science (e.g., Curran et al., 2020; Wieler, 2002), and many processes and reservoirs have been characterized through their study (Fig. 1). Exogenous processes include impacts by asteroids, comets, and smaller particles (e.g., Füre et al., 2012, 2015, 2018), solar wind sputtering (e.g., Grimberg et al., 2006), and bombardment by high-energy cosmic ray radiation (e.g., Eugster et al., 2006). Radioactive decay and diffusion comprise the only endogenic processes known to currently affect noble gas concentrations and distribution within the lunar regolith (Füre et al., 2018). Additionally, in many lunar regolith samples, the measured concentration of ^{40}Ar is too great to be explained by the in situ decay of ^{40}K and cosmogenic production alone. This remaining ^{40}Ar is termed “parentless” (i.e., the parent isotope concentration does not support in situ production of this gas) and is thought to derive from degassed radiogenic ^{40}Ar from the Moon’s interior that is subsequently ionized by UV radiation and re-implanted into a secondary host sample (Fagan et al., 2014; Manka & Michel, 1970; Poppe et al., 2021).

Of particular interest to this study are contributions from solar wind implanted at the lunar surface, and production of noble gas isotopes by high-energy particles derived from solar and galactic sources. These processes leave a characteristic chemical and isotopic record and can modify (i.e., elementally and isotopically fractionate) previously accumulated records. For example, solar wind implantation (which, for Ne isotopes, exhibits mass-dependent fractionation upon implantation, leading to a depth-dependent range of compositions; Grimberg et al., 2006) simultaneously adds to the noble gas inventory of a sample, and (along with micrometeorite impacts) causes sputtering of the grain surface. This sputtering results in the loss of a variable fraction of the mass-dependent fractionated Ne (due to the loss of the grain surface to a depth where the gas was implanted) and gives rise to a range of measured “trapped” Ne endmember isotopic ratio compositions (e.g., Grimberg et al., 2006). We adopt the term “sputtering affected implantation-fractionated solar wind” (SAIF-SW) to denote gas compositions resulting from this process, although we are keen to impress upon readers that this is not a distinct component. These records can be used to constrain the duration a lunar sample has been exposed to the cosmic ray flux and the parameters of its exposure (e.g., Bogard et al., 1971), specifically establishing the duration of a sample’s exposure time near the surface

(e.g., Eugster et al., 2006; Joy et al., 2011) and its shielding (or burial depth) history (e.g., Lorenzetti et al., 2005; Reedy et al., 1979) if gas loss (e.g., the effects of shock and diffusion) can be excluded. Additionally, noble gas species can be used to analyze the solar wind flux and composition throughout solar system history (e.g., Grimberg et al., 2008; Heber et al., 2003; Thiemens & Clayton, 1980).

Cosmogenic noble gases are produced in lunar samples by two distinct particle fluxes. First, SCR is produced by the Sun, ranges in energies up to a few hundred MeV (Lewis, 2004), and decreases in flux intensity with increasing distance from the Sun. GCR is extrasolar in origin, with typical energies around 10^{10} eV but ranging up to 10^{21} eV (Lewis, 2004), and is considered isotropic (i.e., the radiation flux intensity is homogenous irrespective of the incident angle). The lower limit of GCR energies is controlled by the breaking effect of solar radiation on these particles as they pass through the heliopause (i.e., GCRs are modulated by solar output; thus, the GCR flux is subject to variation in line with the periodic variation of solar output; Potgieter, 2013). However, these variations average out over a few million years (Poluianov et al., 2018; Rao et al., 1994). Because of their lower energies, SCRs have shorter penetration depths (only a few cm into the lunar regolith), while GCRs penetrate much deeper (≥ 1 m, and up to 5 m in lunar soil; Heiken et al., 1991; see also Füre et al., 2020).

The exogenous processes, detailed in Fig. 1, aid the development of a regolith blanket layer via a combination of bedrock breakup (i.e., comminution; fragmentation of rock into finer fragments) and agglutination (i.e., impact melt fusing of regolith grains into agglutinates; Lucey et al., 2018; McKay et al., 1986; Spray, 2016). Impacts also distribute the fragments of rock far across the lunar surface, as well as vertically throughout the regolith. It is the impact-driven “gardening” that is responsible for the regolith at any one place on the Moon showing different durations of exposure to space (e.g., Curran et al., 2020). These differences represent the effects of impacts occurring at different times, and the different amounts of ejecta contributed to the sampled area by any given impact. Critically, the burial depth of any given regolith component is likely to have changed repeatedly throughout its history, due to the impact statistics of the lunar surface as well as secondary ballistic regolith redistribution (Costello et al., 2018). These shielding changes can have significant effects on the “true” CRE history of a sample (i.e., the actual exposure conditions experienced by the sample over its history), and in many cases, these effects are obscured in the “apparent” history of a sample (i.e., the effects the calculation

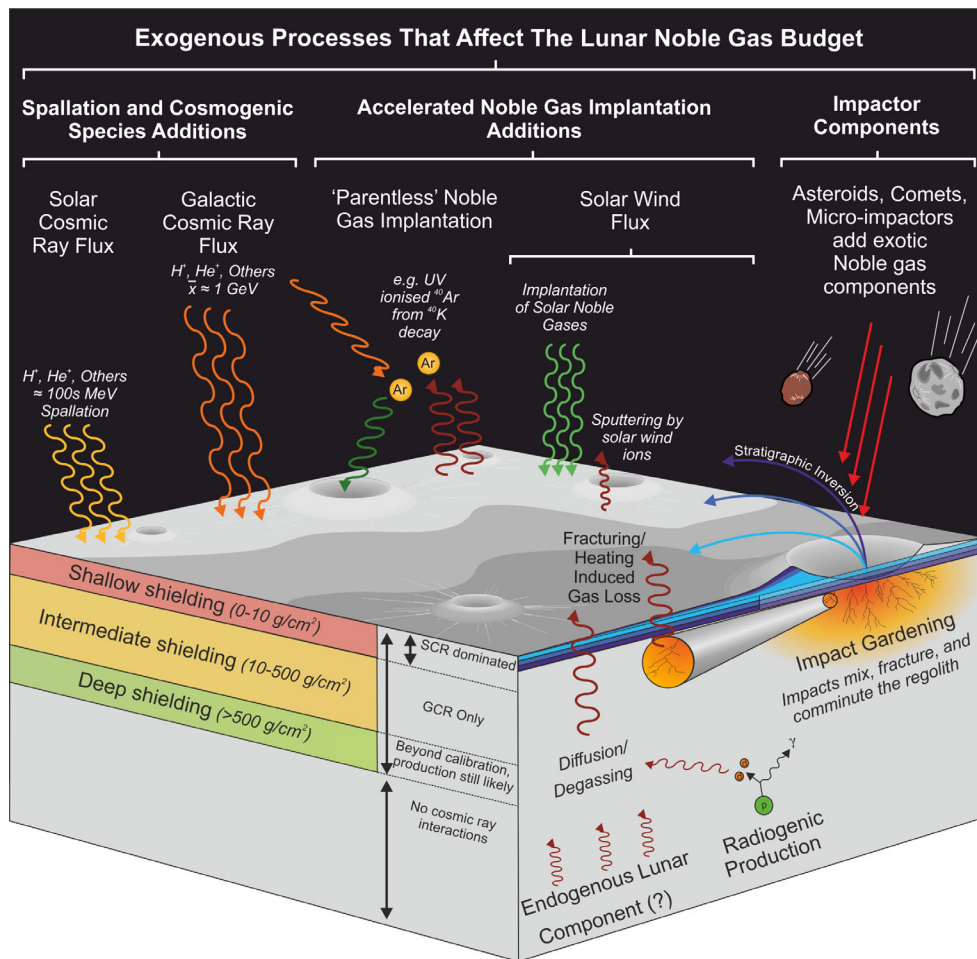


Fig. 1. Schematic diagram of the processes that affect noble gas distribution and concentration on the Moon. (Color figure can be viewed at wileyonlinelibrary.com.)

model has the resolution to reveal) because of the necessary simplifications made during CRE model calculations. It is a limitation of the data that the complex history must be modeled using a very small number of stages. In this work, we exploit the known presence of the sample at the surface when it was collected to deconvolute the record into a period of surface exposure and a period of exposure at depth characterized by an average depth and an exposure time. There is also, of course, a third period of nonexposure since the samples are almost certainly much older than the total CRE age.

The rate at which an individual regolith fragment is “gardened” depends on its residence depth(s). Recent work by Costello et al. (2018) shows that by including secondary impacts (i.e., those derived from projectiles of an initial impact on the Moon’s surface), the turnover rate may be significantly higher than previously estimated (e.g., depths of ~1 cm reworked to homogenization within 100,000 yr). The result of this reprocessing is a well-mixed regolith, where a given soil

sample may contain various fragments of lunar rock, each of which potentially experienced a distinct record of astronomical and geological phenomena. The noble gas record of these events preserved in an individual particle is a convolution of signatures of separate processes and, in some cases, has been subject to partial erasure by impact heating and particle sputtering (Burgess & Stroud, 2018; Greer et al., 2020). This complexity presents a challenge to deciphering the space exposure history of a single lunar regolith sample (e.g., Bhandari et al., 1972; Lorenzetti et al., 2005). Methods that enable the CRE history of a sample to be investigated with greater resolution, such as the one presented here, could potentially benefit our understanding of these regolith evolution processes.

Apollo 12 Landing Site, Previous Studies, and Current Geological Perspectives

The Apollo 12 landing site is situated on the edge of Surveyor crater (3.01239°S, 23.42157°W; Davies &

Colvin, 2000), located on the southeastern side of the Oceanus Procellarum (Fig. 2). Several nearby large (~tens of km diameter) craters contributed ejecta to the local area, including Copernicus (Copernican age), Reinhold (Eratosthenian age), and Lansberg (Upper Imbrian age) (Barra et al., 2006). The emplacement of ejecta would have (a) introduced the fragments of high-temperature impact melt to the local area, possibly causing thermal blanketing effects (Fernandes & Artemieva, 2012); and (b) caused the ballistic sedimentation of the local geology, excavating and mixing fragments of local lava flows into the ejecta blanket deposit (Oberbeck, 1975). Crater counting techniques place the surface age (i.e., the age of surfaces covered by Copernican crater ejecta rays) of the Apollo 12 landing site at $\sim 796 \pm 61$ Ma (Iqbal et al., 2020).

The topography of the immediate Apollo 12 landing site and sampling area is dominated by four sizeable craters—Surveyor crater (SE), Middle Crescent crater (NW), Head crater (WSW), and Bench crater (SW) (Fig. 2). Several smaller unnamed craters are visible in images of the landing site (Fig. 2). Details of each of these local and more distal craters, along with calculated formation ages, are reported in Table 1. The occurrence of benches and large boulders in craters ~3 m deep (e.g., Bench crater; Burnett et al., 1975) has been used to discern that the regolith layer is thin enough for these small craters to have penetrated into the underlying basaltic bedrock (Calio et al., 1970; Stöffler & Ryder, 2001). Additionally, highland ejecta material (mainly from the Imbrian aged Fra Mauro formation) underlies the basalt emplacements of the landing site area. This material also outcrops in islands (i.e., *kīpukas*) ~15–25 km from the landing site. Stöffler and Ryder (2001) explained that the occurrence of these island-like outcrops implies that the basaltic lava flow deposits are quite thin (i.e., tens to hundreds of meters thick).

The Apollo 12 landing site is characterized by several basalt lava flows (~80 m thick in total; Rhodes et al., 1977) from a series of volcanic eruptions (Snape et al., 2018; see also Iqbal et al., 2020). Vertical mixing of these layers via both impact bombardment and regolith gardening may have occurred between the discrete periods of volcanism (Barra et al., 2006). Neal et al. (1994a, 1994b) argue that the two local basalt groups (ilmenite and pigeonite suites) are likely of similar ages (3.15–3.17 Gyr), with two other (olivine and feldspathic) suites being older (~3.22 Gyr), based on petrogenetic evolution models for basalts found at the Apollo 12 landing site. Snape et al. (2018) provide evidence that disputes the exact stratigraphy of these units, although they agree broadly with the range of crystallization ages present within the local lithologies. The sequence suggested by Snape et al. (2018), based on

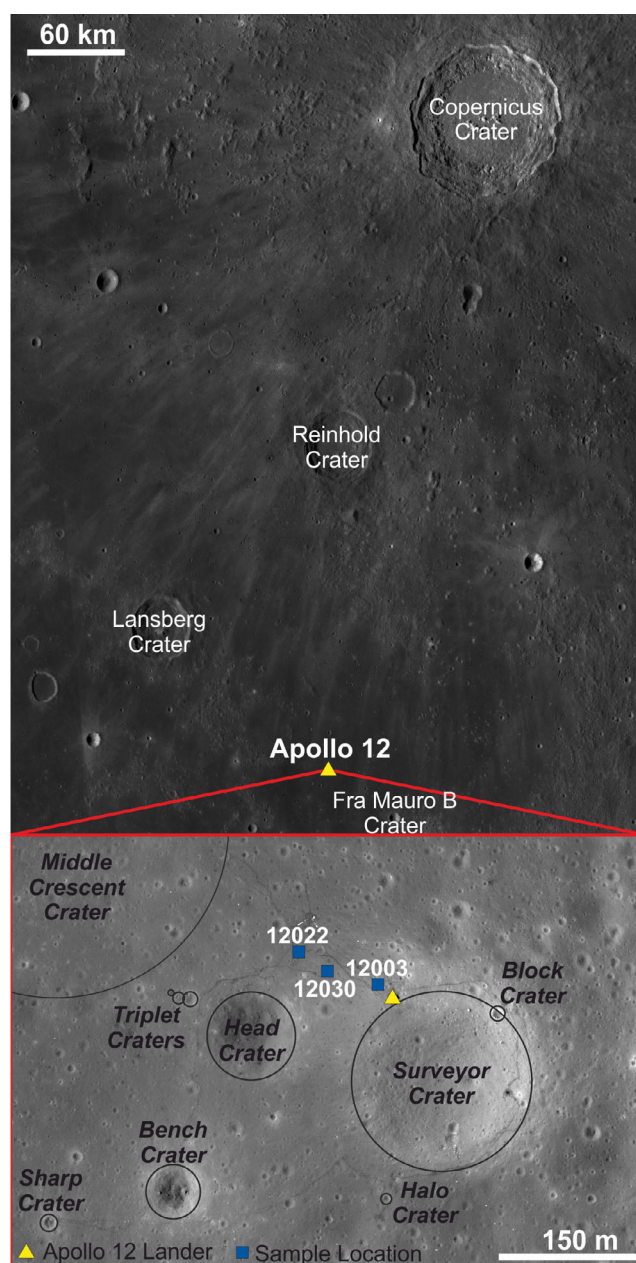


Fig. 2. Selenographic setting of the Apollo 12 landing site, detailing key features of the landing site and sample collection locations for those samples analyzed in this study. Images: (a) mosaic image of LROC WAC regional data 956.4996196,-12.3158115,-6.2652921,13.4173284), (b) LROC NAC image of the local area (image number M168353795 NASA/Goddard Space Flight Center/ASU). (Color figure can be viewed at wileyonlinelibrary.com.)

Pb-Pb isotopic analyses, comprises a young pigeonite basalt unit (3.129 ± 0.01 Ga), followed by an olivine basalt unit (3.163 ± 0.01 Ga), a second pigeonite basalt unit (3.176 ± 0.006 Ga), an ilmenite basalt unit (3.187 ± 0.006 Ga), and finally a possible underlying feldspathic basalt unit (3.242 ± 0.013 Ga).

Table 1. Details of craters within and near the Apollo 12 landing site (see also Figs. 2 and 9b).

Crater	Diameter	Distance to landing site	Formation period (cosmic ray exposure age)
Copernicus	93 km ¹	400 km (N)	Copernican (800 Ma ¹)
Reinhold	48 km ¹	200 km (N)	Eratosthenian
Lansberg	40 km ¹	100 km (NW)	Upper Imbrian
Surveyor	158 m ²	(SE) (~130 m ^a)	Post Copernican (190 Ma ⁵ to 240 Ma ⁴)
Middle Crescent	400 m ³	(NW) (~367 m ^a)	Post Copernican (~300 Ma ^c)
Head	126 m ²	(WSW) (~139 m ^a)	Post Copernican ^b
Bench	46 m ²	(SW) (~308 m ^a)	Post Copernican ^b

^aEstimated distances from the crater center to the collection location of sample 12003. Calculated by this study, using information from Fig. 8b.

^bA range of ages has been proposed interchangeably for these craters: Head crater: 40 Ma⁴, 90–180 Ma⁵, 144 Ma⁶; Bench crater: 90 Ma⁵.

^cThe literature CRE age peak around 300–350 Ma may represent the formation age of Middle Crescent crater, although we note this is conjecture on our part.

¹Barra et al. (2006); ²Davies and Colvin (2000); ³Calio et al. (1970); ⁴Funkhouser (1971); ⁵Wänke et al. (1971); ⁶Bogard et al. (1971).

Although the local units represent a relatively constrained period of basalt eruption, Crawford et al. (2007) note that the Oceanus Procellarum region itself contains a wide range of distinct basaltic units with much more varied crystallization ages from 1.2 to 3.5 Gyr (based on data from Hiesinger et al., 2003; Li et al., 2021; Wilhelms et al., 1987). The younger (i.e., <3.1 Gyr) basalt units do not outcrop in the Apollo 12 landing site area. It is, however, possible that ejecta from impacts on these relatively young basalts may have been deposited across the site (Li & Mustard, 2005). If so, basalt fragments in soil samples from the Apollo 12 mission may sample and allow us to probe this wide range of lava flow diversity.

KREEP-rich basalt material is also abundant in regolith soils from the Apollo 12 site. This material is thought to derive either from surrounding nonmare terrains or from below the Oceanus Procellarum mare basalt flows (i.e., the Fra Mauro formation). Hubbard and Gast (1971) estimated that between 30 and 70% of the regolith around the Apollo 12 site can be classified as this “non-mare” material, with Korotev et al. (2000) further refining that range to 43% (based on the makeup of <1 mm regolith fines). Barra et al. (2006) calculated that the nonmare components were sourced from a mix of the 93 km diameter Copernicus impact crater (adding a regolith layer ~45 cm in thickness), the 40 km diameter Lansberg impact crater (~91 cm ejecta addition), and the 48 km Reinhold crater (~30 cm of ejecta addition); see also Jolliff et al. (2000). Evidence of Copernicus impact ejecta material within the Apollo 12 sample suite primarily comes from the presence of (i) KREEP-rich ropy glass fragments with 1–2.5 Ga formation ages (Wentworth et al., 1994), (ii) partial argon isotopic resetting of igneous rocks between 700 and 800 Ma (Alexander et al., 1976; Barra et al., 2006; Eberhardt et al., 1973), and (iii) samples with radiometric ages of 800–850 Ma (Alexander et al., 1976; Eberhardt et al., 1973; Stöffler & Ryder, 2001). These

ages agree with surface ages based on crater counting techniques which range between 519 and 1210 Ma (Hiesinger et al., 2012). The Alpes Formation (ejecta from the large Imbrium impact basin; Spudis et al., 1988) outcrops ~50 km away from the landing site and serves as a possible local source of some of the nonmare material found at the site (Barra et al., 2006).

SAMPLES AND METHODS

We have adapted well-established methods (e.g., Eugster, 2003; Füre et al., 2018; Lorenzetti et al., 2005) used in noble gas cosmochemistry with the aim of discerning greater detail of a sample’s CRE history and its place within the context of rocks found (both local and introduced) at the Apollo 12 landing site. Our results are compared with calculations carried out using simple single-stage CRE parameters (see the Cosmic Ray Exposure History from Neon Isotopes section).

Lunar Samples

This study focused on a series of 10 small basalt fragments extracted from Apollo 12 soil samples 12003 (nine samples: subsamples 4 × 12003,310, 2 × 12003,311, 1 × 12003,314, 1 × 12003,316, and 1 × 12003,317) and 12030,187 (one subsample). We also analyzed a piece of the hand specimen sample 12022,304 (three subsamples from the same parent rock). The studied samples from soil 12003 are all whole particles from the 2 mm to 1 cm size range subsplit, derived from parent soil 12001, at the lunar surface, close to the Lunar Module on the flank of Surveyor crater (Fig. 2). Based on the sampling tools available to the Apollo astronauts (Allton, 1989), we surmise that every sample was extracted from between approximately 0 and 5 cm depth in the regolith (this may be up to ~10 cm depth if the entire scoop frame was submerged into the soil, but from images of the astronauts testing use of the tools,

in Allton, 1989, this seems unlikely). Soil sample 12030 was collected from the fragmental lining of a 1 m crater on the northeast flank of Head crater (Marvin, 1978). Sample 12030,187 is a coarse-fined subsplit. The studied sample was subdivided from a 5 × 5 mm basalt chip (parent 12030,105). The sample collection locations are shown in Fig. 2 (see also Korotev et al., 2011).

Snape et al. (2014) described the sample preparation techniques and methods used for this sample set. In summary, prior to the study carried out by Snape et al. (2014), the fragments were separated from their respective bulk soil samples at NASA Johnson Space Center. Each of the basalt particles was mechanically broken into two or more aliquots by our team at Birkbeck College London. One aliquot of each mechanically broken particle was used for petrology and bulk chemistry analysis, the methods and findings of which are reported by Alexander (2015), Alexander et al. (2016), and Snape et al. (2014). These chemistry measurements allowed Snape et al. (2014) to classify the samples into their specific origin lava flow types (Table 2). This work uses the bulk chemistries determined by Alexander (2015), Alexander et al. (2016), and Snape et al. (2014) in order to determine the sample-specific concentrations of target elements for spallation-derived noble gas species (of He, Ne, and Ar). This allowed us to model the cosmogenic noble gas production rates specific to each individual particle more accurately (cosmogenic nuclide production rates vary from particle to particle because the target element concentrations vary).

The petrology and bulk chemical analyses of Alexander (2015), Alexander et al. (2016), and Snape et al. (2014) show that the 10 basalt samples have a variety of textures and chemistries and can mostly be classified into recognized Apollo 12 basalt groups. The basalt type nomenclature used here follows the scheme adopted by Snape et al. (2014, 2018) and Alexander et al. (2014, 2016). Olivine, pigeonite, and ilmenite type basalts are based on the scheme of Neal and Taylor (1992) and Neal et al. (1994a). An additional feldspathic basalt type was proposed for sample 12003,314 by Snape et al. (2014) based on similarities to sample 12038, but this was ultimately refuted by Alexander et al. (2016) due to differences in the plagioclase chemistry of these samples. Instead, Alexander et al. (2016) argued that 12003,314 is likely representative of an evolved pigeonite basalt.

Analytical Procedures

Noble gases were measured in fragments of each basalt grain, of masses between 3 and 75.6 mg (12003,310: 1A = 18.8 mg, 2A = 24.4 mg, 3C = 4.8 mg,

Table 2. Sample details and likely craters of origin.

Sample	Textural type ¹	Basalt type	CRE age group ¹	Excavation crater ^c
12003,310,1A	Type 2	Olivine ¹	Group 2	Surveyor
12003,310,2A	Type 2	Olivine ¹	Group 1	Head
12003,310,3C	Type 2	Olivine ¹	Group 2	Surveyor
12003,310,4C	Type 2	Olivine ¹	Group 1	Head
12003,311,1A	Type 4	^a	Group 2	Surveyor
12003,311,2A	Type 4	^a	Group 2	Surveyor
12003,314,C	Type 1	^b	Group 4	Nonlocal
12003,316,A	Type 4	^a	Group 3	Nonlocal
12003,317,C	Type 5	Pigeonite ¹	Group 4	Nonlocal
12030,187,C	N/A	Olivine ²	Group 3	Nonlocal
12022,304	N/A	Ilmenite ³	Group 12022	Middle Crescent

Cosmic ray exposure age groups: Group 1 = ~120 Myr, Group 2 = ~200 Myr, Group 3 = >440 Myr, Group 4 = Production rates cannot be calculated.

^aSnape et al. (2014) suggested these samples represent slowly cooled basalts from a previously unrecognized low-Ti lava flow or a subsurface magma chamber.

^bDefined originally as feldspathic (Snape et al., 2014), but later revised to evolved pigeonite (Alexander et al., 2016).

^cThis assumes the cosmic ray exposure age corresponds to the formation age of a single impact crater, which brought the sample to within the reach of the cosmic ray flux, prior to its eventual exhumation onto the lunar surface.

¹Snape et al. (2014); ²Alexander et al. (2016); ³Neal et al. (1994b).

4C = 4.2 mg; 12003,311: 1A = 20.3 mg, 2A = 9.2 mg; 12003,314,C = 15.1 mg; 12003,316,A = 75.6 mg; 12003,317,C = 6.4 mg; 12030,187,C = 3.0 mg; 12022 chip = 20.29 mg; debris = 0.97 and 0.86 mg). Masses were selected based on the aliquots available after the mechanical fracturing of each original basalt grain. Samples were wrapped in Al foil and gases were extracted in four temperature steps (700, 1000, 1400, and 1700 °C) for 20 min in a double-walled ultra-high vacuum furnace. For some samples, a re-extraction of the final step (1700 °C) was performed in order to ensure that the samples were fully degassed. Step pyrolysis allows the separation of surface-correlated components (e.g., noble gases adsorbed from terrestrial air or implanted solar wind) from volume-correlated components (e.g., noble gases produced by cosmic ray interactions; e.g., Palma et al., 2002).

The released gases were purified by exposure to three hot GP50 ZrAl alloy getters for 20 min and the heavy noble gases (Ar, Kr, and Xe) were absorbed onto liquid nitrogen-cooled charcoal. The Ne was subsequently trapped on charcoal at -243 °C for 20 min. The helium was expanded into the mass spectrometer and its abundance and isotopic composition determined. During the final stages of He analysis, the Ne was released at -173 °C for 15 min, then analyzed. The heavy noble gases were subsequently

desorbed from the nitrogen-cooled charcoal by heating to room temperature for 15 min prior to Ar isotope determination.

The He, Ne, and Ar isotopic compositions and abundances were determined in a MAP 215-50 mass spectrometer in static mode, using established procedures (Codilean et al., 2008; Györe et al., 2015). ^4He , ^{36}Ar , ^{38}Ar , and ^{40}Ar were measured on a Faraday detector with an amplifier equipped with a $10^{11} \Omega$ resistor. ^3He , ^{20}Ne , ^{21}Ne , and ^{22}Ne were measured on a Burle channeltron electron multiplier in pulse counting mode at 2.5 kV. The hydrogen partial pressure was minimized by a room temperature GP50 getter in the mass spectrometer source volume. Liquid nitrogen-cooled charcoal was used to minimize the heavy noble gases, hydrocarbons, and CO_2 in the mass spectrometer during the analysis of He and Ne isotopes. Ne isotope measurement procedures, including management of isobaric interferences, are reported in Codilean et al. (2008).

Mass spectrometer sensitivity and mass fractionation corrections were determined by repeated analysis of aliquots of the HESJ international standard for He (Matsuda et al., 2002) and an air reservoir for Ne and Ar isotopes. Empty Al foil packets were heated at all temperature steps and abundances considered to be representative of process blanks. Except for the reheating steps (see Table 3 for the temperature of these reheating steps), the blank values never exceeded 0.5% of the measured gas concentrations. Where isotope abundances and ratios are reported, the quoted uncertainty is at the 1σ level.

RESULTS

The noble gas data are presented in Table 3 (a complete table of data is available in Table S2 in the supporting information). Uncertainties are 1σ and include measurement errors and standard reproducibility. With the exception of sample 12030,187, noble gas concentrations and isotopic ratios fall within the typical range for lunar crystalline rocks (based on comparison to data collated by Curran et al., 2020). Sample 12030,187 has between 3 and 10 times higher gas concentrations than other samples measured in this study. For this sample, the measured concentrations of noble gas isotopes are within the range expected for Apollo 12 lunar regolith samples (Curran et al., 2020). Surface implanted components (e.g., implanted parentless radiogenic ^{40}Ar and solar wind gases) are evolved at lower temperatures, for all samples (He: <700 °C; Ne and Ar: 700 – 1000 °C). Sample 12022,304 did not release any significant surface implanted gases due to the difference in sample type (the fragment measured was sourced from inside the hand specimen rock). Cosmogenic noble gases

and a fraction of radiogenic ^{40}Ar dominate the gases released at higher temperatures (see also Fig. S2 in the supporting information).

We visualize the Ne data on three-isotope plots (Fig. 3) to define the contributions of different processes (solar, cosmogenic, terrestrial atmosphere contamination). The data define a vector along which each measurement corresponds to varying proportions of a binary component gas mixture. This vector is limited at either end by “endmember” values (i.e., the composition of a pure sampling of one component of the binary component gas mixture). The endmember components we define here are the “trapped component” (consistent with a mixture of solar wind and SAIF-SW; e.g., Füri et al., 2018) and the “cosmogenic component” (governed by a range of parameters; sample chemistry, burial depth, and cosmic ray flux, among others: e.g., Hohenberg et al., 1978; Lorenzetti et al., 2005). The Ne isotope endmember values for each sample are reported in Table S3 in the supporting information. The range of “trapped” $^{20}\text{Ne}/^{22}\text{Ne}$ observed in our samples is from 12.36 ± 0.02 to 13.70 ± 0.01 (with an assumed $^{21}\text{Ne}/^{22}\text{Ne}$ ratio between 0.029 and 0.033). Two samples (12003,316,A and 12003,314,C) yield lower “trapped” $^{20}\text{Ne}/^{22}\text{Ne}$ ratios of 10.21 ± 0.03 to 10.97 ± 0.02 ; however, we note that the gas inventories of these samples are dominated by the cosmogenic component and, thus, these calculated “trapped” component values are less reliable (Figs. 3g and 3i). The cosmogenic $^{21}\text{Ne}/^{22}\text{Ne}$ range observed is from 0.61 ± 0.002 to 0.94 ± 0.003 (see Fig. S1 in the supporting information for details on the calculation of these composition values, Fig. S3 in the supporting information for a comparison of all Ne releases according to heating step temperature, and Table S4 in the supporting information for a table of the mixing line parameters for each sample).

Deconvolving the contribution of cosmogenic ^{40}Ar to a sample’s overall ^{40}Ar budget is complicated by the variable abundance of radiogenic and “parentless” ^{40}Ar (see the Noble Gas Reservoirs and Interactions with the Lunar Surface section). This “parentless” ^{40}Ar component is in high enough (but variable) concentration to prevent our deconvolution method from being used to independently identify Ar isotopic endmembers, without the introduction of an additional endmember component into the otherwise binary composition gas mixture. The exclusion of ^{40}Ar limits the number of Ar isotopes that can be adopted for a method similar to that which we use for Ne isotope deconvolution. The restriction to two Ar isotopes means the endmember compositions cannot be meaningfully constrained. We, therefore, adopt the Ar deconvolution approach of Füri et al. (2018) for these data. For

Table 3. Noble gas concentrations and isotopic ratios measured in the Apollo 12 basalt sample set. Uncertainties reported are 1 σ confidence interval.

Sample	Mass Mg	Temperature °C	²⁰ Ne 10 ⁻⁶ cm ³ STP g ⁻¹	³⁶ Ar	²⁰ Ne/ ²² Ne	²¹ Ne/ ²² Ne	⁴⁰ Ar/ ³⁶ Ar	³⁸ Ar/ ³⁶ Ar
12022,304,1a	20.29	700	0.01239 ± 0.00001	0.00482 ± 0.00002	0.8134 ± 0.0010	0.8162 ± 0.0013	276.91 ± 1.115	1.4258 ± 0.0065
		1000	0.04425 ± 0.00003	0.00834 ± 0.00002	0.8319 ± 0.0006	0.8979 ± 0.0008	166.974 ± 0.407	1.5401 ± 0.0038
		1400	0.05648 ± 0.00002	0.04629 ± 0.00004	0.8434 ± 0.0004	0.9155 ± 0.0005	27.132 ± 0.032	1.5823 ± 0.0013
		1700	0.00027 ± 0.00001	0.00066 ± 0.00001	1.6983 ± 0.0096	0.7826 ± 0.0062	120.212 ± 0.222	1.3383 ± 0.0033
		1700	n.d.	0.0001 ± 0.00001	-	-	301.852 ± 42.063	0.2274 ± 0.032
Total		0.33769 ± 0.00270	0.18414 ± 0.00020	0.8365 ± 0.0067	0.8973 ± 0.0101	67.978 ± 0.089	1.559 ± 0.0018	
12030,187,C	3.0	700	7.80927 ± 0.01437	1.36147 ± 0.00067	11.701 ± 0.0219	0.0919 ± 0.0002	4.886 ± 0.003	0.1825 ± 0.0003
		1000	1.99002 ± 0.00097	1.2926 ± 0.00087	5.1824 ± 0.0024	0.4571 ± 0.0003	3.067 ± 0.003	0.2064 ± 0.0003
		1400	1.07155 ± 0.00291	0.5414 ± 0.00050	2.49 ± 0.0068	0.7283 ± 0.0027	15.656 ± 0.017	0.9356 ± 0.0011
		1700	0.0017 ± 0.00002	0.00095 ± 0.00021	3.7645 ± 0.0349	0.5259 ± 0.0068	132.788 ± 29.257	0.6791 ± 0.1496
		Total		25.02748 ± 0.20022	9.38875 ± 0.00558	7.3357 ± 0.0587	0.3715 ± 0.0042	6.013 ± 0.004
12003,310,1A	18.8	700	0.51602 ± 0.00072	0.08552 ± 0.00002	11.542 ± 0.0160	0.1103 ± 0.0002	18.155 ± 0.048	0.2164 ± 0.0002
		1000	0.16813 ± 0.00093	0.03737 ± 0.00002	4.9657 ± 0.0274	0.5623 ± 0.0043	40.006 ± 0.034	1.366 ± 0.0008
		1400	0.03097 ± 0.00004	0.01668 ± 0.00004	1.1457 ± 0.0014	0.8707 ± 0.0014	46.948 ± 0.118	1.2809 ± 0.003
		1700	0.00036 ± 0.00001	0.00048 ± 0.00001	1.1592 ± 0.0044	0.837 ± 0.0045	146.513 ± 1.731	1.3429 ± 0.0046
		1700	0.00008 ± 0.00001	n.d.	3.4402 ± 0.2831	0.2377 ± 0.0276	-	-
Total		2.21914 ± 0.01775	0.42961 ± 0.00014	6.7554 ± 0.0538	0.451 ± 0.0051	28.125 ± 0.021	0.6539 ± 0.0003	
12003,310,2A	24.4	700	0.50083 ± 0.00040	0.07943 ± 0.00002	11.738 ± 0.0096	0.1128 ± 0.0001	15.631 ± 0.005	0.2209 ± 0.0002
		1000	0.13975 ± 0.00042	0.03911 ± 0.00002	4.2713 ± 0.0128	0.6363 ± 0.0026	24.42 ± 0.016	0.2772 ± 0.0003
		1400	0.03325 ± 0.00002	0.01707 ± 0.00004	1.077 ± 0.0006	0.8853 ± 0.0007	38.45 ± 0.087	1.1833 ± 0.0027
		1700	0.00245 ± 0.00001	0.00033 ± 0.00001	0.8648 ± 0.0031	0.9247 ± 0.0046	104.188 ± 0.397	1.4759 ± 0.0071
		1700	n.d.	0.00014 ± 0.00002	-	-	397.157 ± 56.980	0.3783 ± 0.0545
Total		2.04617 ± 0.01637	0.41665 ± 0.00021	6.1992 ± 0.0496	0.5095 ± 0.0057	21.623 ± 0.014	0.361 ± 0.0003	
12003,310,3C	4.8	700	0.60563 ± 0.00101	0.05339 ± 0.00005	13.365 ± 0.0214	0.0666 ± 0.0001	22.4 ± 0.025	0.2139 ± 0.0004
		1000	0.26741 ± 0.00013	0.09351 ± 0.00003	6.3992 ± 0.0033	0.4772 ± 0.0003	15.068 ± 0.005	0.2403 ± 0.0002
		1400	0.05949 ± 0.00003	0.0414 ± 0.00001	1.7693 ± 0.0009	0.8265 ± 0.0005	26.708 ± 0.023	0.6546 ± 0.0003
		1700	0.00126 ± 0.00000	0.00066 ± 0.00001	1.0878 ± 0.0017	0.861 ± 0.0019	162.637 ± 0.276	0.6494 ± 0.0023
		Total		2.87154 ± 0.02297	0.57082 ± 0.00019	7.6611 ± 0.0610	0.4245 ± 0.0048	20.202 ± 0.014
12003,310,4C	4.2	700	0.57958 ± 0.00042	0.04779 ± 0.00005	11.866 ± 0.0084	0.068 ± 0.0001	36.761 ± 0.046	0.2226 ± 0.0004
		1000	0.2259 ± 0.00034	0.09445 ± 0.00006	6.0994 ± 0.0093	0.4986 ± 0.0010	17.911 ± 0.025	0.2431 ± 0.0002
		1400	0.05197 ± 0.00004	0.0407 ± 0.00003	1.544 ± 0.0012	0.8431 ± 0.0009	31.864 ± 0.035	0.6834 ± 0.0008
		1700	0.00072 ± 0.00001	0.00065 ± 0.00001	0.8247 ± 0.0139	0.8351 ± 0.0199	447.23 ± 31.580	0.7413 ± 0.0045
		Total		2.61503 ± 0.02092	0.54925 ± 0.00018	7.1266 ± 0.0569	0.4227 ± 0.0047	27.43 ± 0.026
12003,311,1A	20.3	700	0.08855 ± 0.00009	0.01679 ± 0.00002	9.8756 ± 0.0098	0.2198 ± 0.0003	36.288 ± 0.050	0.4831 ± 0.0011
		1000	0.04608 ± 0.00004	0.01298 ± 0.00002	1.2248 ± 0.0012	0.8784 ± 0.0011	41.143 ± 0.076	0.9467 ± 0.0017
		1400	0.03921 ± 0.00003	0.02195 ± 0.00004	0.8563 ± 0.0006	0.8993 ± 0.0008	22.788 ± 0.041	1.4681 ± 0.0026
		1700	0.00062 ± 0.00001	0.00048 ± 0.00001	0.97 ± 0.0036	0.8869 ± 0.0046	152.361 ± 0.700	1.4056 ± 0.0047
		1700	0.00008 ± 0.00001	n.d.	1.7244 ± 0.0938	0.5922 ± 0.0455	-	-
Total		0.51712 ± 0.00414	0.15793 ± 0.00015	1.8754 ± 0.015	0.8251 ± 0.0093	32.878 ± 0.040	1.0211 ± 0.0012	

Table 3. *Continued.* Noble gas concentrations and isotopic ratios measured in the Apollo 12 basalt sample set. Uncertainties reported are 1σ confidence interval.

Sample	Mass Mg	Temperature °C	^{20}Ne $10^{-6}\text{ cm}^3\text{ STP g}^{-1}$	^{36}Ar	$^{20}\text{Ne}/^{22}\text{Ne}$	$^{21}\text{Ne}/^{22}\text{Ne}$	$^{40}\text{Ar}/^{36}\text{Ar}$	$^{38}\text{Ar}/^{36}\text{Ar}$	
12003,311,2A	9.2	700	0.24216 ± 0.00039	0.0052 ± 0.00001	13.154 ± 0.0208	0.0389 ± 0.0001	23.486 ± 0.034	0.2329 ± 0.0004	
		1000	0.31242 ± 0.00020	0.06042 ± 0.00004	6.5151 ± 0.0042	0.4814 ± 0.0004	22.408 ± 0.021	0.3791 ± 0.0004	
		1400	0.05392 ± 0.00004	*	1.0694 ± 0.0009	0.8932 ± 0.0010	*	*	*
		1700	0.00042 ± 0.00001	0.00044 ± 0.00001	2.0043 ± 0.0194	0.6741 ± 0.0092	215.371 ± 0.669	0.4477 ± 0.0016	
		Total	1.90935 ± 0.01527	*	5.2045 ± 0.0417	0.5896 ± 0.0066	*	*	
12003,314,C	15.1	700	0.0654 ± 0.00005	0.00325 ± 0.00002	6.1132 ± 0.0045	0.4397 ± 0.0004	64.353 ± 0.378	0.5047 ± 0.0057	
		1000	0.12648 ± 0.00018	0.04037 ± 0.00002	2.6809 ± 0.0038	0.7342 ± 0.0014	56.517 ± 0.069	0.8274 ± 0.0005	
		1400	0.11325 ± 0.00004	0.07862 ± 0.00004	0.8731 ± 0.0003	0.8824 ± 0.0004	16.455 ± 0.011	1.5206 ± 0.0007	
		1700	0.00031 ± 0.00001	0.00115 ± 0.00001	1.7044 ± 0.0043	0.7553 ± 0.0026	149.106 ± 0.166	1.0521 ± 0.0017	
		Total	0.94069 ± 0.00753	0.37587 ± 0.00020	1.6268 ± 0.0130	0.8198 ± 0.0092	32.122 ± 0.017	1.2627 ± 0.0008	
12003,316,A	75.6	700	0.16107 ± 0.00019	0.03377 ± 0.00002	5.5209 ± 0.0067	0.4828 ± 0.0008	18.873 ± 0.014	0.5294 ± 0.0006	
		1000	0.15339 ± 0.00007	0.02507 ± 0.00002	1.2902 ± 0.0006	0.8981 ± 0.0005	25.995 ± 0.022	0.8402 ± 0.0008	
		1400	0.13439 ± 0.00012	0.03701 ± 0.00004	0.8609 ± 0.0008	0.926 ± 0.0011	10.248 ± 0.012	1.5394 ± 0.0016	
		1700	0.00129 ± 0.00000	0.00278 ± 0.00001	0.8531 ± 0.0014	0.9185 ± 0.0021	13.411 ± 0.007	1.5785 ± 0.0009	
		1700	n.d.	0.00003 ± 0.00001	—	—	48.471 ± 6.745	1.4024 ± 0.1972	
Total	1.03607 ± 0.00829	0.30167 ± 0.00024	1.4726 ± 0.0118	0.8728 ± 0.0098	17.302 ± 0.016	1.0171 ± 0.0009			
12003,317,C	6.4	700	0.39412 ± 0.00078	0.04384 ± 0.00002	11.057 ± 0.0220	0.1272 ± 0.0003	27.378 ± 0.013	0.4621 ± 0.0003	
		1000	0.09879 ± 0.00004	0.0343 ± 0.00002	2.7325 ± 0.0010	0.7289 ± 0.0004	12.949 ± 0.007	0.5516 ± 0.0003	
		1400	0.06052 ± 0.00007	0.05667 ± 0.00006	0.9518 ± 0.0012	0.8628 ± 0.0014	14.978 ± 0.020	1.454 ± 0.0024	
		1700	0.00028 ± 0.00001	0.00037 ± 0.00001	2.0832 ± 0.0097	0.6245 ± 0.0422	416.869 ± 1.721	0.685 ± 0.003	
		Total	1.71207 ± 0.01370	0.41313 ± 0.00022	4.0861 ± 0.0327	0.6333 ± 0.0071	19.599 ± 0.019	0.9012 ± 0.0005	
12022(S2)	0.969	700	0.05372 ± 0.00006	0.03397 ± 0.00001	0.8313 ± 0.0010	0.864 ± 0.0014	279.08 ± 0.309	0.6687 ± 0.0008	
		1700	0.05349 ± 0.00013	0.05683 ± 0.00006	0.8794 ± 0.0022	0.8975 ± 0.0031	63.956 ± 0.091	1.4344 ± 0.0022	
		1800	0.00374 ± 0.00003	0.02179 ± 0.00001	7.7065 ± 0.0594	0.0377 ± 0.0004	309.635 ± 0.378	0.2015 ± 0.0003	
		Total	0.3384 ± 0.00271	0.34228 ± 0.00021	0.881 ± 0.0070	0.877 ± 0.0099	176.405 ± 0.159	0.9648 ± 0.0017	
		700	0.01003 ± 0.00007	0.01577 ± 0.00002	0.9788 ± 0.0065	0.7606 ± 0.0071	334.733 ± 0.507	0.4698 ± 0.0011	
12022(S1)	0.856	1000	0.04406 ± 0.00010	0.00983 ± 0.00002	0.8295 ± 0.0020	0.8706 ± 0.0029	223.32 ± 0.466	1.7352 ± 0.0037	
		1400	0.04311 ± 0.00008	0.04386 ± 0.00004	0.8588 ± 0.0015	0.9071 ± 0.0022	49.888 ± 0.064	1.5997 ± 0.0023	
		1700	0.00264 ± 0.00002	0.001 ± 0.00000	1.5983 ± 0.0125	0.7218 ± 0.008	26.301 ± 0.039	3.561 ± 0.0101	
		Total	0.3045 ± 0.00244	0.21423 ± 0.00016	0.8666 ± 0.0069	0.8746 ± 0.0098	137.502 ± 0.131	1.3937 ± 0.0028	
		700	0.01003 ± 0.00007	0.01577 ± 0.00002	0.9788 ± 0.0065	0.7606 ± 0.0071	334.733 ± 0.507	0.4698 ± 0.0011	

n.d.—No gas was measured above the background blank (for measured concentrations). Where no ratio can be subsequently calculated, a dash (—) is used to denote no value.

*Data not available due to technical measurement error during this heating step.

components where shielding depth indicators are a necessary component, we adopt the values from our Ne deconvolution method calculations.

Cosmic Ray Exposure History from Neon Isotopes

The data reduction process we use to calculate cosmogenic Ne isotope concentrations is depicted in the flow diagram provided in the supporting information (Fig. S1). Repeat extractions at the final temperature step released small amounts of gas (<1% of any one isotope of Ne released) and were excluded from the data treatment. A mixing line was fit to the remaining stepwise heating data ($^{21}\text{Ne}/^{22}\text{Ne}$ versus $^{20}\text{Ne}/^{22}\text{Ne}$) for each sample by minimizing the square of the Mahalanobis distance (a statistical measure of the distance of each point from a modeled linear regression distribution) between the modeled line and the data (using the technique of Gilmour, 2017). The resulting parameters calculated by the Mahalanobis fit software can be found in Table S4. The uncertainties of the mixing line coefficients were estimated from the scatter of points around the line. The parameters of the mixing line, combined with the release that had the lowest $^{20}\text{Ne}/^{22}\text{Ne}$ ratio (i.e., the highest proportion of cosmogenic gas), then provided a constraint on the bulk composition of cosmogenic neon in the sample. This approach avoided the introduction of the bias inherent in assuming values for either the cosmogenic or noncosmogenic endmember gas compositions. Any given trapped endmember value was calculated as the intercept between the sample mixing line, and a tie-line between a solar wind composition and an arbitrary SAIF-SW value, from the mass-dependent fractionation line of solar wind (i.e., this value was used to extrapolate an unlimited mixing line between a solar wind composition and an undefined SAIF-SW endmember). For each sample, the composition of this noncosmogenic “trapped” component determined from the mixing line was always consistent with a variably fractionated solar wind component. We combined the bulk sample chemistries for each of the samples (Table S1 in supporting information) (Alexander et al., 2014; Snape et al., 2014) and theoretical Ne production rates (Hohenberg et al., 1978) to calculate sample-specific Ne production rates as a function of depth. When these rates are combined as ratios ($^{21}\text{Ne}/^{22}\text{Ne}$ versus $^{20}\text{Ne}/^{22}\text{Ne}$), they result in a curve that defines the limits of variation with depth of the theoretical total (i.e., inclusive of SCR and GCR reaction contributions) cosmogenic Ne gas compositions for the sample (e.g., Fig. 4b; see also Fig. S1). This theoretical curve was then combined with the fit to our data to constrain the shielding depth(s) experienced by the sample. We then

combined the production rate(s) corresponding to these shielding depths with the concentrations of cosmogenic isotopes to determine exposure ages.

Single-Stage Cosmic Ray Exposure Modeling

We first considered the simplest case, where the sample was exposed to cosmic rays at a single shielding depth (i.e., the apparent shielding depth scenario in Fig. 4a) for a period of time (the exposure duration). In this scenario, we assume that for the rest of the sample’s history, it was buried so deep that cosmogenic nuclide production was negligible (i.e., an apparent buried exposure duration of 0 Myr), or surface exposure was short enough to be considered negligible (i.e., an apparent surface exposure duration of 0 Myr). The nominal burial depth of such an exposure is determined from the intersection of the line fitted to our data with the theoretical production curve calculated based on the chemistry of the specific sample (Fig. 4b: label 3). This allows the concentration of the cosmogenic component and its shielding depth (in this model) to be determined. The cosmogenic nuclide production rate appropriate to the calculated single-stage shielding depth can then be used to calculate a CRE age (calculations for each sample are reported in Table 4). Single-stage CRE ages calculated using ^{21}Ne show a range of ages between 122 ± 12 Ma and 468 ± 47 Ma. Similar calculations using ^{38}Ar broadly agree with the ^{21}Ne CRE ages, although we note a difference in calculated CRE ages between the applied Ne and Ar systems for some samples. Disparities in the calculated CRE ages may either indicate gas loss (i.e., preferential degassing of Ne isotopes relative to Ar isotopes resulting in a partial loss of cosmogenic isotopes from the Ne system) or inaccurate cosmogenic nuclide production rate modeling (i.e., differences between the adopted sample chemistry and the actual aliquot sample chemistry, resulting in the calculation of a cosmogenic nuclide production rate curve that is inaccurate for chemistry of the measured sample). For example, sample 12003,310,1A shows evidence of extreme Ne gas loss (observable in the ^{38}Ar CRE age of 615 ± 62 Ma compared to the ^{21}Ne CRE age of 158 ± 16 Ma). However, the disagreement between the CRE ages of the sample 12022 aliquots—12022,S1: $^{21}\text{Ne} = 300 \pm 30$ Ma, $^{38}\text{Ar} = 348 \pm 35$ Ma (agreement between both CRE ages); and 12022,S2: $^{21}\text{Ne} = 329 \pm 33$ Ma, $^{38}\text{Ar} = 225 \pm 23$ Ma (disagreement between both CRE ages)—highlights a likely limitation to our knowledge of the precise aliquot bulk chemistry caused by their low aliquot masses. It is likely that the aliquot-labeled 12022,S2 did not have Ar spallation target element concentrations that were representative of the bulk sample chemistry, given how

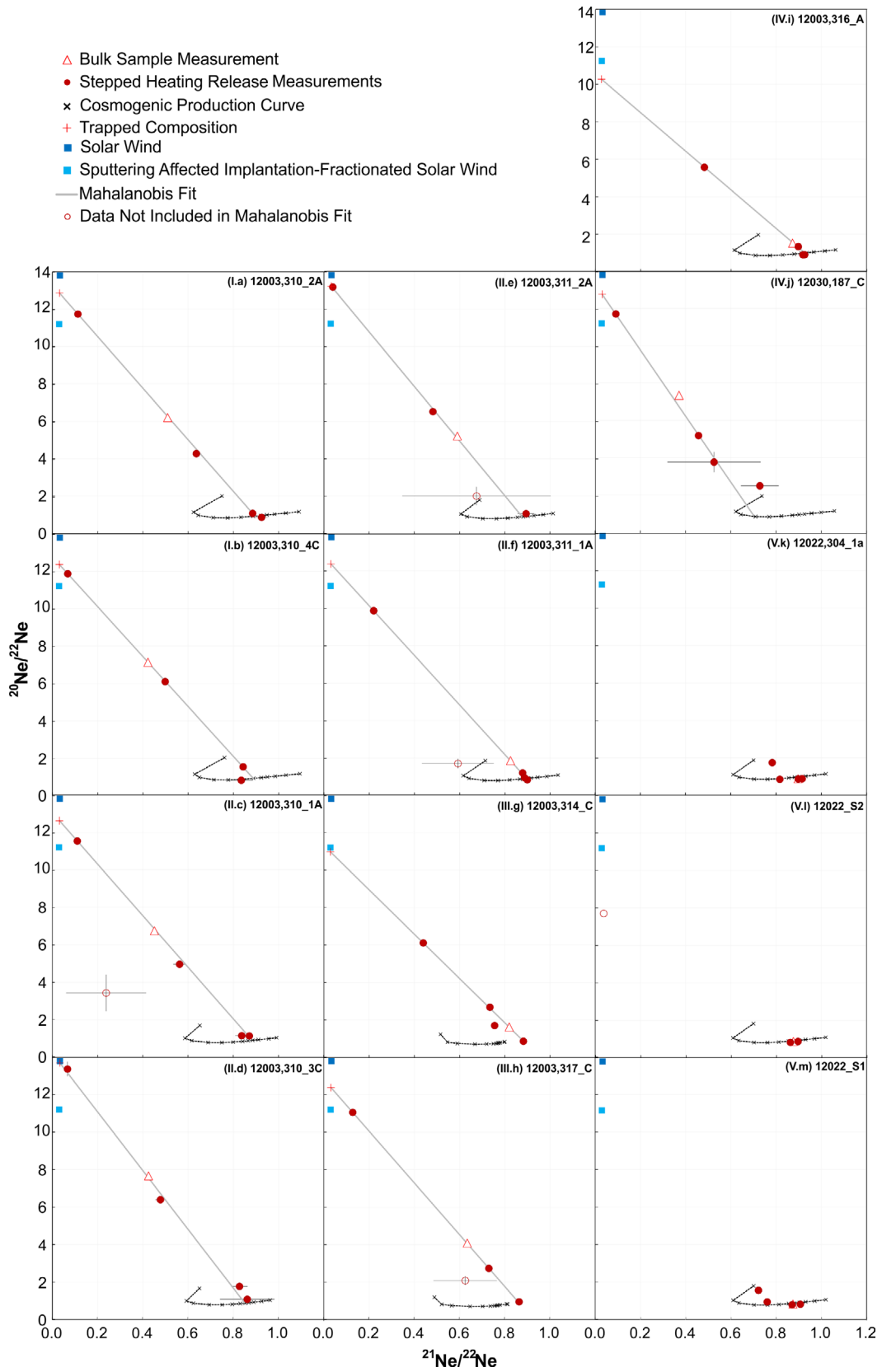


Fig. 3. Stepwise Ne isotope data for each sample. The data are sensitivity corrected. Blank correction was unnecessary. Each plot also shows the theoretical range of possible cosmogenic components specific to each sample; these curves are calculated using chemistry data from Snape et al. (2014) and Alexander et al. (2016) and production rate models of Hohenberg et al. (1978). Bulk sample measurement refers to the isotopic ratio representative of a summed total gas inventory for the sample. A Mahalanobis fit is a modeled linear regression where the line parameters are dictated by an algorithm that minimizes the Mahalanobis distance (a statistical measure of the distance of each point from the linear regression distribution) of each data point within the data set. See Table S4 for the calculated Mahalanobis fit mixing line parameters, and their associated uncertainty, for each sample. Uncertainties on the mixing lines are on the order of 10^{-2} for gradients and intercepts. Correlation coefficients show moderate to good fit (i.e., >0.56) of the models to the measured data. (Color figure can be viewed at wileyonlinelibrary.com.)

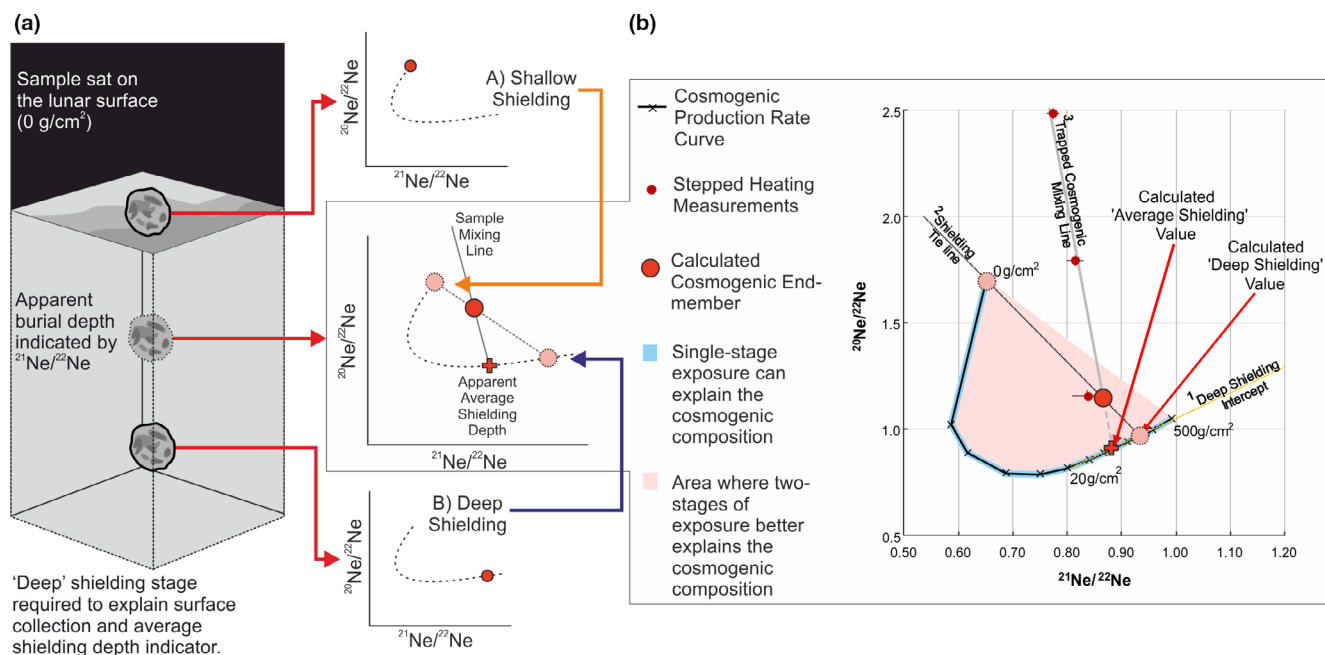


Fig. 4. a) An illustration explaining the regolith positions represented by the two-stage exposure model. b) Schematic illustration of the calculation of both the two-stage exposure model and the calculation of the average shielding depths (¹calculated as a straight line extrapolated from the two closest production rate model depths; ²a theoretical tie-line that allows two-stage exposure, calculated by extrapolating a line from 0 g cm⁻² through the cosmogenic endmember, to its intercept with the theoretical production rate curve; ³the sample-specific mixing line, calculated as a least squares fit of the measured data, this line is extrapolated to its intercept with the theoretical production rate curve to calculate the average shielding depth). (Color figure can be viewed at wileyonlinelibrary.com.)

it compares to the larger mass chip (12022,304_1a: ²¹Ne = 363 ± 37 Ma, ³⁸Ar = 343 ± 34 Ma), which agrees with all CRE ages of 12022,S1 and the ²¹Ne CRE age of 12022,S2, but disagrees with the ³⁸Ar CRE age of 12022,S2; this is discussed further in the Sample Mineralogical Homogeneity section.

Two-Stage Cosmic Ray Exposure Modeling

The principle of dividing the CRE history of a sample into multiple stages is not new. Burnett et al. (1975) used the depth dependence of cosmogenic ¹³¹Xe/¹²⁶Xe to construct two-stage CRE models in order to examine samples thought to be related to Bench crater. Although our technique is comparable to that used by Burnett et al. (1975), we note that the assumptions (i.e., critically the required assumptions relating to the

duration of exposure) are significant. As noted by Burnett et al. (1975), CRE histories corroborated by multiple techniques are ideal when investigating the complex evolution of the lunar regolith at a site such as the Apollo 12 landing site. Additionally, our technique is ideal for investigating the small craters that (presumably) occurred more recently, but are not sufficiently deep to have excavated material that was otherwise deeply shielded from exposure to the cosmic ray flux. Eugster et al. (1984) similarly use the cosmogenic ¹³¹Xe/¹²⁶Xe ratio as a depth indicator, in order to construct two-stage CRE histories for a set of samples. These previous studies undoubtedly have benefits, but we note that (given current technological constraints on in situ sample heating capabilities) our technique is perhaps suitable for in situ analyses (this will be discussed later).

As this Apollo 12 sample set was collected within ~5 cm of the surface (see the Lunar Samples section), at least part of each sample's cosmogenic noble gas budget was produced at a negligible shielding depth. For this reason, we have developed a "two-stage" CRE model (see Figs. 4 and S1 for details).

For any sample, the depth dependence of the theoretical production rate ratios ($^{21}\text{Ne}/^{22}\text{Ne}$ and $^{20}\text{Ne}/^{22}\text{Ne}$) defines a curve that depends on its chemistry (see Table S1). In principle, a sample's bulk cosmogenic composition represents a sum of compositions corresponding to the burial depths it has experienced since its formation. The contribution to the sum from each burial depth depends on the production rate at that depth and the duration of the sample's exposure at that depth (i.e., the "apparent" shielding depth is a product of the time the sample was exposed at "deep" shielding depths, and the time the sample was exposed on the surface, indicated in Fig. 4a). It is possible to explain any calculated cosmogenic endmember composition with more than one modeled shielding history since the number of stages of "deep" shielding is unconstrained. When modeling any calculated cosmogenic endmember composition as a product of multiple stages of shielding, it is necessary to constrain the number of stages permitted based on the number of constraining isotopes available to the model. Without this constraint, multiple conflicting modeled histories may be asserted to explain the calculated cosmogenic endmember of a sample. In these models, any given stage of a sample's shielding history is a sum of the exposure effects experienced by the sample during that stage (where those contributions affect the sample according to the interrelation between cosmogenic nuclide production rates, the duration of exposure, and the given sample shielding depth). For a three-isotope model to have significance, it is necessary to constrain the model to two stages, and additionally, either the duration of exposure or the depth at which that exposure occurred must be assumed for one of the stages of modeled exposure. Here, we restrict samples to two stages of exposure, one at $>10\text{ g cm}^{-2}$ depth and one at 0 g cm^{-2} . We construct a tie-line between the composition at 0 g cm^{-2} and the point on the sample-specific mixing line corresponding to the lowest measured $^{20}\text{Ne}/^{22}\text{Ne}$ ratio (the release most dominated by cosmogenic neon). We then extrapolate this tie-line until it intercepts the calculated production rate curve to deduce the $^{21}\text{Ne}/^{22}\text{Ne}$ production rate at the assumed second, deeper, exposure depth. From this, the production rate (and corresponding exposure time) at this depth can be calculated. We thus divide each sample's shielding history (i.e., the duration and depths a sample existed at over its CRE history) into two

distinct stages, constraining one of those stages to 0 g cm^{-2} (Fig. 4b: label 2). We compare the results from this approach to those from a single-stage model to gain insights into the ability of noble gas analysis to constrain near-surface exposure history.

Note that we cannot currently progress the model to investigate shielding depths beyond the radiation length of 500 g cm^{-2} due to the limited calibrated range of the production rate model data of Hohenberg et al. (1978). We expect that the drop-off in production rate at these depths is rapid but also note that, at shielding depths of 500 g cm^{-2} , production rates are still comparable to a few percent of the production rates at the lunar surface (i.e., 0 g cm^{-2}). Given that these basalts were erupted ~3.2 Gyr ago (i.e., the length of time since these rocks crystallized in their parent lava flows), we cannot discount measurable cosmogenic nuclide production at shielding depths greater than 500 g cm^{-2} within our samples. We accept this as a limitation of our method and find that data from two samples may plausibly be explained by irradiation at burial depths exceeding 500 g cm^{-2} (see Figs. 3g and 3h).

For a measured composition of cosmogenic Ne, our two-stage model yields a concentration of cosmogenic Ne produced at no shielding (0 g cm^{-2}), and the concentration and production depth of a second cosmogenic component. For the latter component, we can work out the shielding depth and hence production rate. It, thus, produces a duration of surface CRE, and a duration and depth of a buried period of CRE.

Derivation of Apollo 12 Basalt Sample Exposure Histories Based on Our Data

The results of applying our one- and two-stage CRE models to the Apollo 12 sample data are presented in Tables 4 and 5, respectively. We consider each sample's history to potentially consist of any combination of (1) a period of "deep" burial shielded from production of isotopes by cosmic ray interaction; (2) a period over which it has been present in the "intermediate" near-surface environment where cosmogenic production of noble gas isotopes can proceed; (3) a period of exposure at the "surface" (the region from which the parent soil was collected). Figure 1 shows the interrelation of these three burial zones, and how they relate to cosmic ray flux penetration. The samples we have analyzed fall into four distinct exposure age groups.

Group 1—12003,310,2A and 12003,310,4C: ~120 Myr in the Near-Surface Environment

For these samples, the data point with the highest proportion of cosmogenic Ne lies within error of the theoretical production curve. Because of this, only a "single-stage" model is appropriate despite the

Table 4. Calculated single-stage CRE ages and shielding parameters. Uncertainties reported are 1 σ confidence interval.

	Cosmogenic gas fraction concentrations		Average shielding depth g cm ⁻²	Single-stage exposure age for average shielding depth (Hohenberg et al., 1978)		Single-stage exposure age for average shielding depth (Leya et al., 2001)
	²¹ Ne 10 ⁻⁶ cm ³ STP g ⁻¹	³⁸ Ar		²¹ Ne CRE age Myr	³⁸ Ar CRE age	²¹ Ne CRE age
12003,310_1A	0.1430 ± 0.0012	0.2215 ± 0.00015	105	157.9 ± 15.9	615.2 ± 61.5	104.4 ± 10.5
12003,310_2A	0.1635 ± 0.0006	0.0690 ± 0.00005	46	126.3 ± 12.6	107.9 ± 10.8	93.1 ± 9.3
12003,310_3C	0.1528 ± 0.0004	0.0746 ± 0.00004	65	169.9 ± 17.0	138.4 ± 13.8	102.5 ± 10.3
12003,310_4C	0.1489 ± 0.0004	0.0745 ± 0.00004	47	122.4 ± 12.2	112.0 ± 11.2	87.4 ± 8.7
12003,311_1A	0.2268 ± 0.0022	0.1284 ± 0.00237	68	194.1 ± 19.5	206.7 ± 21.0	137.4 ± 13.8
12003,311_2A	0.2124 ± 0.0011	^b	53	171.1 ± 17.1	^b	123.2 ± 12.3
12003,316_A	0.6127 ± 0.0062	0.2337 ± 0.00405	88	467.6 ± 47.0	550.5 ± 55.9	340.2 ± 34.2
12022(S2)	0.3368 ± 0.0040	0.1905 ± 0.00116	60	329.2 ± 33.2	225.1 ± 22.6	224.3 ± 22.6
12022(S1)	0.3073 ± 0.0036	0.2949 ± 0.00166	58	299.5 ± 30.2	348.4 ± 34.9	204.8 ± 20.6
12022,304_1a	0.3622 ± 0.0043	0.2905 ± 0.00048	79	362.6 ± 36.5	343.4 ± 34.4	251.7 ± 25.3
12030,187_C	^c					
12003,314_C	^a					
12003,317_C	^a					

^aShielding depth cannot be calculated because the gas mixing line does not intercept the theoretical cosmogenic nuclide production rate ratio curve. Therefore, no cosmic ray exposure ages can be calculated for these samples.

^bCalculation not possible due to measurement error during one heating step of the analysis.

^cCosmogenic ²¹Ne here is calculated as having a composition based on a single exposure at a depth corresponding to one of two intercept points. Using the Hohenberg et al. (1978) model: 0.59 g cm⁻² yields 1.217 ± 0.005 × 10⁻⁶ cm³ STP g⁻¹ and a corresponding CRE age of 515.5 ± 51.6 Myr; 4.75 g cm⁻² yields 1.214 ± 0.005 × 10⁻⁶ cm³ STP g⁻¹ and a corresponding CRE age of 1138.6 ± 114.0 Myr. Using the Leya et al. (2001) model: 0.59 g cm⁻² yields a CRE age of 1049.3 ± 105.0 Myr and 4.75 g cm⁻² yields a CRE age of 922.0 ± 92.3 Myr. ³⁸Ar CRE ages are similarly calculated as a single exposure at those given shielding conditions: a cosmogenic ³⁸Ar concentration of 1.478 ± 0.002 × 10⁻⁶ cm³ STP g⁻¹ yields single-stage CRE ages of: 634.4 ± 63.4 Myr (at 0.59 g cm⁻²) and 2750.4 ± 275.1 Myr (at 4.75 g cm⁻²), both calculated using the Hohenberg et al. (1978) model.

likelihood that these samples have a more complicated exposure history (i.e., it is expected that small lunar basalt fragments have generally undergone processes, such as comminution, burial, and exhumation, that affected the cosmogenic nuclide production rate the sample experienced). Two-stage modeling results in a period of surface exposure within error of zero, and the parameters of the deep burial stage are close to those of the single-stage model.

The data suggest that these samples have had ~120 Myr of exposure at relatively shallow depths (~40–50 g cm⁻²). Our interpretation of this group is that these samples likely formed and were held at depths beyond the reach of significant cosmic ray flux (i.e., >1 m), before being ejected by an impact event at ~120 Ma. This age is coincident with the currently accepted approximate age of Head crater (144 Myr; Wänke et al., 1971). Impact excavation then brought these samples up to the surface (i.e., 0–5 g cm⁻²). Surface emplacement must be recent enough that the concentration of cosmogenic isotopes produced during this surface exposure cannot be distinguished from the sample's remaining noble gas

budget. Based on the maximum ratio between the shallow and deep shielded exposure durations (see the Resolving Two Stages of Exposure section), we estimate a maximum surface exposure of <120,000 yr.

Group 2—12003,310,1A; 12003,310,3C; 12003,311,2A; and 12003,311,1A: 170–200 Myr in the Near-Surface Environment

The second cluster consists of four samples. Three of the chips in this group (12003,310,1A; 12003,310,3C; and 12003,311,2A) have cosmogenic neon releases (i.e., the lowest ²⁰Ne/²²Ne ratio) that do not lie on the theoretical production line (Figs. 3c–f). Therefore, our two-stage model can be applied to these samples. Modeled two-stage exposure indicates a period of exposure on the lunar surface of 6 ± 2 to 7 ± 2 Myr, and a period of deeper shielded exposure lasting ~170–200 Myr. The most spallation-rich measurement from sample 12003,311,1A lies on the theoretical production curve, leading to a well-constrained near-surface residence time of 194 ± 20 Myr.

The data for this group are consistent with samples that were shielded from the cosmic ray flux until around

Table 5. Two-stage cosmic ray exposure modeling results. Uncertainties reported are 1 σ confidence interval.

	Cosmogenic gas fraction	“Deep” stage shielding depth	Shallow exposure stage	Deep exposure stage	Total exposure
	^{21}Ne $10^{-6} \text{ cm}^3 \text{ STP g}^{-1}$	g cm^{-2}	^{21}Ne CRE age Myr	^{21}Ne CRE age	^{21}Ne CRE age
12003,310_1A	0.1430 ± 0.0012	188	6.4 ± 1.5	179.9 ± 19.4	186.3 ± 19.5
12003,310_2A	0.1635 ± 0.0006	43	<0.1*	126.1 ± 13.4	126.1 ± 13.4
12003,310_3C	0.1528 ± 0.0004	147	7.0 ± 1.9	190.7 ± 20.5	197.7 ± 20.6
12003,310_4C	0.1489 ± 0.0004	45	<0.1*	122.6 ± 15.6	122.6 ± 15.6
12003,311_1A	0.2268 ± 0.0022	58	<0.2*	187.2 ± 19.5	187.2 ± 19.5
12003,311_2A	0.2124 ± 0.0011	95	6.1 ± 2.2	176.3 ± 19.3	182.3 ± 19.4
12003,316_A	0.6127 ± 0.0062	76	<0.4*	447.6 ± 47.6	447.6 ± 47.6

*Calculated upper limit of surface exposure duration according to Fig. 8.

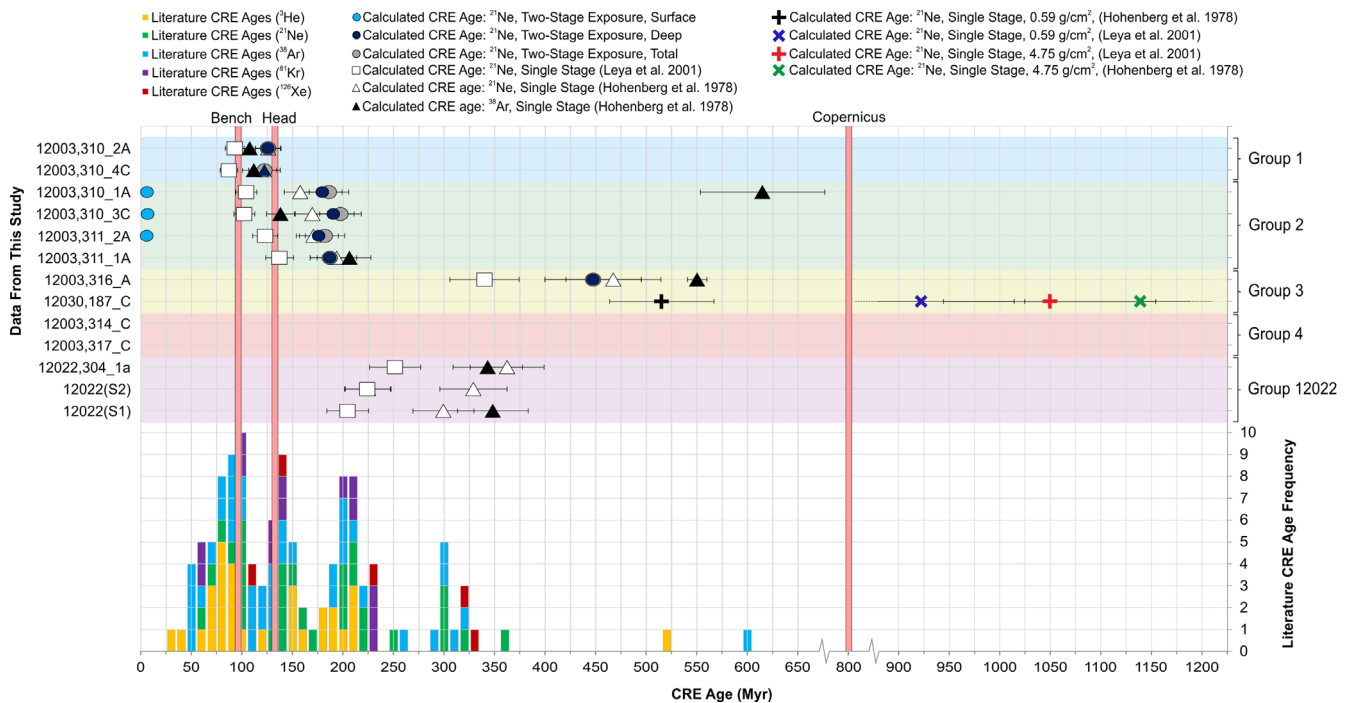


Fig. 5. Cosmic ray exposure age values calculated for our samples from (a) conventional single-stage exposure models (at either the average calculated shielding depth, or at 0 g cm^{-2}) and (b) two-stage exposure models (one period of surface exposure and one period of exposure at depth). Literature data: He: 30 reported ages [a,b,c,e], Ne: 30 reported ages [a,b,c,e], Ar: 39 reported ages [a,b,c,d,e], Kr: 14 reported ages [a,b,e,f,g], Xe: 5 reported ages [c]. These were collated using the database compiled by Curran et al. (2020) (inclusive of references: [a] Bogard et al., 1971; [b] Eugster et al., 1984; [c] Funkhouser, 1971; [d] Füre et al., 2015; [e] Hintenberger et al., 1971; [f] Marti & Lugmair, 1971; [g] Mortimer et al., 2015). The cosmogenic endmember for sample 12030,187,C is poorly defined by the measured data (i.e., the most cosmogenic nuclide-rich gas release results in a ratio that plots outside of the bounds defined by the theoretical cosmogenic nuclide production rate ratio curve for that sample). Calculation of these CRE ages is performed as a simple single-stage exposure at one of two depths, defined by the possible intercepts of the sample mixing line, as described in the text. (Color figure can be viewed at wileyonlinelibrary.com.)

190 Ma ago, then exposed at varying depths before being brought to the lunar surface in the last few million years in two or more separate events. This cluster may relate to a peak in reported Apollo 12 landing site crystalline rock literature CRE ages that centers around 200 Myr (Fig. 5). Sample 12003,311,1A

appears to have been excavated more recently from a shallower depth than the other three, but was likely brought into the near-surface environment at around the same time, suggesting a degree of vertical mixing occurs during exhumation, assuming the samples in this group were exhumed by a single impact.

Group 3—12003,314,C and 12003,317,C: Deep Burial or Heterogeneous Sample Aliquots

For these samples, the modeled endmember mixing line does not intercept the predicted cosmogenic nuclide production rate curve (Figs. 3g and 3h). Where these cosmogenic endmembers plot, relative to the curve produced by the predicted cosmogenic nuclide production rates, may suggest shielding conditions greater than 500 g cm^{-2} (e.g., the sample may have been deeply buried). However, the trend of the predicted production rate ratios suggests a constant ratio (for $^{20}\text{Ne}/^{22}\text{Ne}$ and $^{21}\text{Ne}/^{22}\text{Ne}$) may be achieved at a depth beyond the range calibrated for in the adopted model. Therefore, attempts to extrapolate the modeled curve to noncalibrated depths, to calculate the shielding depth of each of these samples, would lead to excessive uncertainty. Thus, the shielding depths of these samples cannot accurately be defined here. Mineralogical or chemical heterogeneity between the aliquot used for noble gas analysis and the aliquot used for bulk chemical analysis may be responsible for this group's nonconformity with the predicted cosmogenic nuclide production rate curve: This issue is discussed further in the Sample Mineralogical Homogeneity section. It is notable that in the theoretical production rate modeling calculation (i.e., Fig. S1c), the calculated maximum $^{21}\text{Ne}/^{22}\text{Ne}$ ratio for these samples (~ 0.8) is markedly lower compared to the other samples (typically ~ 1 or higher; see Fig. 3, and compare the theoretical production rate curves for [g] and [h], to other examples within that figure). It is possible that the adopted composition for this sample and the composition of the aliquot measured for noble gas concentrations were different. The consistency of the calculated theoretical production rate curve (which is based on chemistry data from a different subsplit aliquot) with the shape of the plagioclase curve shown in Fig. 6b supports the possibility of the chemistry aliquot being unrepresentatively enriched in plagioclase, compared to the noble gas aliquot. Additionally, we note the gas inventories of these samples are dominated by their cosmogenic component (a feature that leads to their "trapped" composition being poorly constrained). It is possible that this group represents relatively new 2 mm to 1 cm grains (i.e., they were very recently more deeply shielded in a larger rock or boulder). This would explain the low abundance of solar wind-derived "trapped" gases.

Group 4—12003,316,A (and Plausibly 12030,187,C): >350 Myr in the Near-Surface Environment

The CRE ages of these samples are greater than those previously published for Apollo 12 samples (Fig. 5). Data from sample 12003,316,A are consistent with single-stage exposure for 467 ± 47 Myr. Sample 12030,187,C has a cosmogenic endmember (i.e., its most

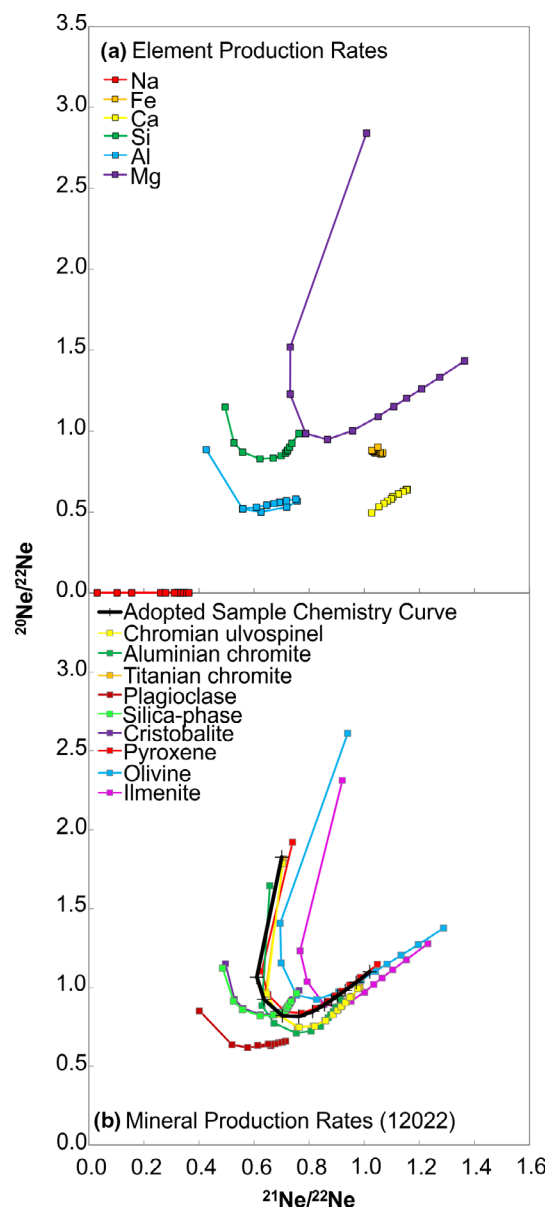


Fig. 6. a) Calculated theoretical spallation production rate ratio curves for elements that produce Ne isotopes, based on data from Hohenberg et al. (1978). b) Calculated theoretical production rate curves for minerals within sample 12022, based (where possible) on the average composition of available measured mineral chemistries (Mineral: n = No. of samples, from [Ref.]) (Plagioclase: n = 1: [a], 2 [b]; Pyroxene: n = 3 [a], 16 [b]; Cristobalite: n = 1 [a]; Silica phase: 1 [a]; Ilmenite: 1 [a], 1 [c]; Olivine: 2 [a], 4 [b], 1 [d], 13 [e]; Aluminian chromite: n = 1 [c]; Titanian chromite: 1 [a]; Chromian ulvospinel: 1 [a], 1 [c]). [a] Weill et al., 1971; [b] Alexander et al., 2014, Alexander, 2015; [c] Cameron, 1971; [d] Brett et al., 1971; [e] Butler, 1972). (Color figure can be viewed at wileyonlinelibrary.com.)

spallation gas rich release) with a $^{20}\text{Ne}/^{22}\text{Ne}$ ratio significantly higher than can be explained by the mixing of modeled shielding depth-dependent cosmogenic

components specific to the sample. Extrapolation of the mixing line intersects the model at two points (Fig. 3j) corresponding to two depths (0.6 and 4.7 g cm^{-2}) that correspond to ages of $516 \pm 36 \text{ Myr}$ and $1139 \pm 121 \text{ Myr}$, respectively. These ages bracket the currently accepted formation age of the Copernicus impact crater (Barra et al., 2006: $782 \pm 21 \text{ Ma}$; Eberhardt et al., 1973: $800 \pm 40 \text{ Ma}$; Alexander et al., 1976: $800 + 400/-50 \text{ Ma}$ based on degassing indicators). It is, therefore, possible that it is a fragment introduced with ejecta from the Copernicus formation event (Barra et al., 2006; Wentworth et al., 1994), but it is also possible that this sample was brought into the near-surface environment at the same time as 12003,316, A. Alternatively, sample 12003,316,A may be a member of “group 3,” but have an aliquot bulk chemistry that is more accurately represented by the adopted bulk chemistry measurements (i.e., it may represent a very recently formed grain, sourced from a larger more deeply shielded rock or boulder).

The failure of data from 12030,187,C to approach the modeled composition of cosmogenic Ne is a consequence of mixing with solar Ne. Sample 12030,187,C is very gas rich, containing an order of magnitude greater concentrations of ^{20}Ne and ^{36}Ar than any other sample measured within this study. However, the bulk $^{20}\text{Ne}/^{22}\text{Ne}$ ratio is within the range of the other samples, suggesting that both cosmogenic and solar gas contributions are elevated; this is consistent with a prolonged period of residence in the near-surface environment.

Crystalline Hand Specimen Sample 12022,304

Sample 12022,304, was measured as three separate sample aliquots: a single chip and two aliquots of mineral debris created during the aliquoting process (see masses in Table 3). The analysis of the chip aliquot yielded a much deeper average shielding depth than the debris samples (chip: 79 g cm^{-2} , compared with debris: 58 and 60 g cm^{-2}). The CRE ages of these aliquots are not within error of each other (Chip: ^{21}Ne $363 \pm 37 \text{ Myr}$ ^{38}Ar $343 \pm 34 \text{ Myr}$, Debris: ^{21}Ne $300 \pm 30 \text{ Myr}$ ^{38}Ar $348 \pm 35 \text{ Myr}$ and ^{21}Ne $329 \pm 33 \text{ Myr}$ ^{38}Ar $225 \pm 23 \text{ Myr}$). See the Sample Mineralogical Homogeneity section for more discussion.

DISCUSSION

Our aim is to examine the evolution of lunar regolith in the Apollo 12 landing site region (Barra et al., 2006; Iqbal et al., 2020; Korotev et al., 2011; Snape et al., 2018) and to assess the viability of using basalt fragments from regolith soils to more effectively probe the geological and astronomical history of the

Moon (Alexander et al., 2016; Crawford et al., 2007, 2021; Snape et al., 2014). To achieve these aims, we discuss several factors that affect the calculation and interpretation of CRE ages (see the Sample Mineralogical Homogeneity section), before going on to discuss implications for the evolution of the Apollo 12 landing site (see the Geological Evolution of the Apollo 12 Landing Site section).

Consideration of Assumptions Used to Calculate Cosmic Ray Exposure Histories

Sample Mineralogical Homogeneity

This work combines element-specific theoretical production rates of Ne isotopes and chemical compositions specific to the fragment of each measured sample to derive theoretical production rate ratios.

The regolith chips analyzed here were prepared in such a way that each sample was split in two, with one half used to establish the sample chemistry (Alexander et al., 2014, 2016; Snape et al., 2014) and the other half to derive the noble gas abundances reported in Table 3. Thus, in our use of the chemical measurements to calculate each sample’s production rate curve, we have to make an assumption that both halves of the same sample are chemically identical (and likely to, thus, be mineralogically identical). However, we accept that as the samples are crystalline basalts, there might be some sample heterogeneity (mineral size, crystal clumping effects) that would undermine this assumption. For aliquots several times larger than the typical size of a sample’s largest minerals, the effect is likely to be small.

In Fig. 6, we illustrate the cosmogenic Ne isotope compositions for each target element, and each of the constituent minerals (in sample 12022,304) in order to assess the effects this heterogeneity may have on the accuracy of a modeled theoretical cosmogenic nuclide production rate curve. By utilizing the repeat measurements of the sample (three separate aliquots were analyzed: 12022,304,1a; 12022,304,S1; and 12022,304,S2) and the CRE durations and shielding depths calculated for these measurements (Table 4), we infer that sample aliquot heterogeneity (e.g., in small mass samples) has likely significantly affected how reliably the modeled production rate curves can be applied to the small mass aliquots (12022,304,S1 and 12022,304,S2).

Two of the measured aliquots are composed of debris resulting from the fracturing of the bulk sample into its respective chemistry and noble gas analysis fragments. These aliquots, labeled “S1” and “S2,” are comprised of lower sample masses (<1 mg each), thus are likely to be more sensitive to mineralogical heterogeneities. Due to the compositional reliance of

these aliquots on the fracture characteristics of each mineral, it is possible that the deviation in evolved noble gas compositions between the three measured aliquots of sample 12022,304 derives from mineral composition heterogeneity between each aliquot. Evolved gas ratios with increasing temperature seen in aliquots 12022,304,1a and 12022,304,S1 indicate that these samples were comprised of multiple minerals (or minerals that evolve different compositions of gas over a range of temperatures). 12022,304,S2, on the other hand, shows consistent gas ratio composition, indicating release from an individual mineral or an even release from all minerals contained within the aliquot over each of the temperature steps.

Based on the production curve calculated from the modal mineralogy of sample 12022, our shielding depth calculations indicate “deep” burial at 58, 60, and 79 g cm⁻² for the three aliquots. In addition, the calculated Ne and Ar CRE ages of the two debris aliquots do not agree (12022,S1: ²¹Ne = 300 ± 31 Ma, ³⁸Ar = 348 ± 35 Ma; 12022,S2: ²¹Ne = 329 ± 33 Ma, ³⁸Ar = 225 ± 23 Ma). Comparing these calculated CRE ages to those of sample 12022,304,1a (²¹Ne = 363 ± 37, ³⁸Ar = 343 ± 34 Ma) indicates that the bulk chemistry values for Ne-producing target elements in sample S1 are not representative of the measured sample, and similarly, the Ar-producing target element concentrations in sample 12022,S2 are not representative of the measured aliquot’s bulk chemistry. All these aliquots must have the same CRE history because they were derived from the same small chip of the parent sample (a solid basalt hand specimen). It is, therefore, likely these differences arise from variation of the mineralogy in the three aliquots subject to noble gas analyses. We note that this assertion is in agreement with the findings of Füre et al. (2020). This basalt is composed of small crystals of plagioclase interstitial between more abundant larger sized olivine crystals (Alexander et al., 2014, 2016; Snape et al., 2014). Our expectation is that aliquots composed of fine-grained debris from processing have higher proportions of fine-grained minerals; in this context, it is notable that the composition of cosmogenic Ne derived from these aliquots is close to that derived from the chip. Based on these findings, it is our recommendation that this data analysis technique should only be applied to data collected from adjacent chips (as opposed to sample preparation debris), where material split from the same initial fragment is available to determine chemistry and noble gas isotopic concentrations. In addition, care should be taken to ensure that aliquots selected for analysis are significantly larger than the largest typical grains in the fragment. Where there is sufficient sample material available, repeats of the chemical analysis and

the noble gas analysis should be carried out in order to understand the uncertainty in quantities derived from these heterogeneities.

Snape et al. (2014) state that sample 12003,314 is coarse-grained (0.2–1.1 mm) and that sample 12003,317 has a more granular texture than any other sample in our sample set. This lends plausibility to the hypothesis that the sample preparation method resulted in aliquot heterogeneity, and that this is the reason for the disparities between the modeled theoretical cosmogenic nuclide production rate values and the measurement derived apparent cosmogenic nuclide production rate values. This effect is more likely to have affected these samples due to their coarse-grained nature, compared with other samples in this study.

Cosmogenic Nuclide Production Rates

Cosmogenic nuclide production rates are affected by a wide range of assumed parameters, including cosmic ray flux constancy, accuracy of theoretical cosmogenic nuclide production rate variables, and the models used to calculate their attenuation with depth (see introduction in the Cosmic Ray Exposure History from Neon Isotopes section). Here, we consider each of these assumptions and examine how they affect our CRE duration calculations.

Cosmic ray flux/spectral variation: In general, a constant cosmic ray flux is assumed when calculating a CRE age (see Herzog & Caffee, 2014). It is, however, likely that the intensity and the particle/energy spectrum of the GCR flux have varied over time as the solar system oscillated through the galactic plane and transited around the spiral arms (time scales of ~10s Myr and several hundred Myr, respectively; e.g., Crawford et al., 2021; Shaviv, 2006). In addition, stochastic variations might be expected owing to nearby supernova explosions (e.g., Melott et al., 2017) and variations in the extent of the heliosphere in response to changes in the density of the local interstellar medium (Cohen et al., 2012; Jasinski et al., 2020). Several studies have attempted to quantify this variation as recorded in a range of extraterrestrial sample types (e.g., Bhandari & Padia, 1974; Smith et al., 2019; Wieler et al., 2013). However, these different studies yield discrepant results and, to date, there is no generally agreed model for the variations of the GCR flux over the history of the solar system. Adding further complexity, the SCR flux and energy spectrum are linked to solar cycle activity and, as such, the SCR flux varies on a periodicity of ~11 yr (Sapundjiev et al., 2020). It is likely these variations (and their inversely correlated modulation of the GCR flux) average out over the durations for which these samples were exposed on the lunar surface.

Given the long exposure durations of some of our samples, assumption of a constant cosmic ray flux becomes difficult to justify. However, calculating CRE ages that account for this potential flux change is not possible because we lack both (a) a model of how the cosmic ray flux has changed over the history of the solar system and (b) the absolute timing of when exposure of our samples occurred.

We hypothesize that variation in the intensity of the cosmic ray flux with a constant energy/particle spectrum would presumably lead to variance in the production rates of each isotope (but no change in the production rate ratios). Ultimately, this would result in CRE ages that were variably offset, from their constant flux exposure ages values, as a function of the constant state cosmic ray flux intensity compared to a variable flux unknown reality. Variations in energy/particle spectrum may affect different isotopic systems to different extents because each cosmogenic noble gas nuclide target element has a unique reaction cross section; it is possible that cosmogenic nuclide production rate ratios would change as a function of this spectrum change (Leya et al., 2001). Such variation could also change the relationship between a shielding depth indicator model and the cosmogenic nuclide production rates experienced by the sample. This would be apparent in (a) CRE ages systematically varying between different chronometer systems based on different elements and (b) inaccurate corrections for shielding depth (because, given fixed sample chemistry, the depth-dependent production rates are ultimately derived from the energy spectrum, which affects the production of secondary particles at depth; e.g., Masarik & Reedy, 1994; Reedy et al., 1979).

The issue that we are ultimately faced with is that, for all exposure age calculations, we cannot be sure of (a) the absolute time at which exposure to the cosmic ray flux occurred (i.e., relative to the entire history of that sample, since its crystallization ~3.2 Gyr ago), and (b) the cosmic ray flux characteristics at the time of exposure for that particular sample. All we can do is assume a constant flux, which in reality may or may not be the case. This is further complicated by lunar samples commonly showing histories with complex exposure conditions (i.e., multiple periods of exposure at different times, where those periods are not necessarily consecutive). Therefore, we establish the following caveats to our findings: The results exhibit apparent groups of ages consistent with all group members having been affected by common exposure/exhumation events. If the cosmic ray flux has varied, the timing and extent of this event are uncertain. Additionally, the existence of groups suggests that the effects of any variation in the cosmic ray energy

spectrum on shielding depth correction (and our interpretations of the history of the Apollo 12 landing site) are limited or uniform across this sample set.

Another consideration is the dependence of our results on the accuracy of the variables used within the model we adopt to predict cosmogenic nuclide production rates. Our sample-specific cosmogenic nuclide production rate models are ultimately derived from a priori theoretical predictions based on nuclear properties and the physics of cosmic ray interactions, reported by Hohenberg et al. (1978). Theoretical models often do not fully reflect the complexity observed in empirical data. Thus, some degree of inaccuracy was expected between our modeled theoretical production rate curves and the empirical production rates of each sample. Given that an aim of this study is to compare our findings with those of previous Apollo 12 landing site studies, we applied an estimated 10% uncertainty to the production rates of Hohenberg et al. (1978), in line with the degree of uncertainty common within CRE age calculations. This led to the production rate being the governing uncertainty within our calculations (to such a significant extent, that the uncertainties on calculated values effectively became 10%).

There are presently two dominant 2π irradiation geometry models that are commonly applied to lunar cosmogenic noble gas production rate calculations: Hohenberg et al. (1978) and Leya et al. (2001). While the model of Leya et al. (2001) is more recent (and calculated to higher depth interval resolution), it does not account for the production of cosmogenic nuclides by SCRs. These SCR interactions are particularly important for CREs on (or within ~10 cm of) the lunar surface, where they are the dominant spallogenic particle flux. This is most noticeably observed in the CRE ages calculated for sample 12030,187,C: at ~1 g cm⁻²; Hohenberg et al. (1978) yield an exposure age of 516 ± 52 Myr, whereas use of the Leya et al. (2001) model yields an exposure age of 1049 ± 105 Myr. In comparison, for the deeper burial scenario (i.e., at a shielding depth of 5 g cm⁻²), Hohenberg et al. (1978) yield a CRE age of 1139 ± 114 Myr, and Leya et al. (2001) yield a CRE age of 922 ± 92 Myr. The decrease in the disagreement between the two ages is due to the progressive decline in SCR-induced spallation with the increase in shielding depth. The variable disparity between the calculated exposure ages (presumably) arises from the Hohenberg et al. (1978) model accounting for SCR spallation interactions (these SCR spallation interactions occur at a much higher rate than GCR reactions at this depth, hence the significant reduction in the time it would take to accumulate the calculated cosmogenic nuclide gas concentration). For this reason, we adopted the model of Hohenberg et al.

(1978). It is noted that the model presented by Leya et al. (2001) shows good agreement for the production of ^{21}Ne and ^{22}Ne from Mg. However, the slight difference between the adopted model and that of Leya et al. (2001), for the production of ^{21}Ne and ^{22}Ne from Si, is noted. Comparison of the CRE ages calculated by each of the two models shows that a consistently lower exposure age is calculated when using the model of Leya et al. (2001) (see Table 4). This should be considered when comparing the CRE ages calculated here (using the Hohenberg et al., 1978, model) to ages presented in other studies where the model of Leya et al. (2001) has been used.

Knowledge of the Noble Gas Endmember(s)

We assume that a mixing of two distinct components (i.e., the cosmogenic endmember and the “trapped” endmember) can explain the noble gas inventory of each sample. We acknowledge that additional components, found within lunar materials, may be present in minor concentrations within the gas inventories of our samples. If present, these components are not expected to contribute significantly to the total noble gas inventory of any sample in this study (i.e., components not identified within the scope of this study may be a source of additional uncertainty but, based on the fit of our two-component mixing models to the measured isotopic ratio data, the contribution of this to the overall uncertainty is expected to be small; see Table S4).

Shallow Shielding Depth Assumption

We note that our two-stage model is inflexible to changes in the “shallow” shielding stage depth. The model, as implemented, assumes all exposure during the “shallow” shielding stage occurred at a depth of 0 g cm^{-2} . This equates to the sample sitting on the very surface of the regolith layer in contact with the solar wind, the Earth’s magnetosphere geotail, and lunar exosphere (Saxena et al., 2019). However, prior to collection, our samples may have resided at any depth within the estimated sampling depth of the Apollo samples (up to $\sim 5\text{ cm}$ into the regolith—see the Lunar Samples section). Each modeled stage of shielding represents an integration of cosmogenic nuclide production rates (or exposure conditions) that the sample experienced within the attenuation depth limits defined for that stage of the model (i.e., $0\text{--}5\text{ g cm}^{-2}$ for “shallow” stage shielding and $10\text{--}500\text{ g cm}^{-2}$ for “deep” stage shielding). In reality, it is unlikely that any given sample has solely resided at a “shallow” shielding depth of 0 g cm^{-2} (this is not to say that the sample has not been at 0 g cm^{-2} , but rather that it is unlikely that the sample has only resided at 0 g cm^{-2} , out of a range of

$0\text{--}5\text{ g cm}^{-2}$). Relaxing this requirement to allow a nonzero burial depth for the “shallow” stage would lead to (1) a lower production rate and hence longer duration for the shallow exposure and, because the tie-line would pivot around the constraining point on our mixing line, (2) a deeper burial depth, lower production rate, and hence longer exposure duration for the “deep” stage. The difference in production rate between 0 and 5 g cm^{-2} , for our samples (given dependency on sample-specific chemistry), ranges from 1.5×10^{-9} to $3.4 \times 10^{-9}\text{ cm}^3\text{ STPg}^{-1}\text{ Myr}^{-1}$, so (already short) shallow exposure stages would be longer by a factor of between 2.6 and 3.6 (based on a comparison of the cosmogenic nuclide production rates of ^{21}Ne at 0 g cm^{-2} compared to 5 g cm^{-2} ; combining the data shown in Table S1 and the production rates of Hohenberg et al., 1978).

Variations in the production rate parameters of the shallow exposure stage are generally more extreme (based on what follows). At shallow depths, a relatively small change in shielding depth can result in a significant difference in the rate of cosmogenic nuclide production and subsequent calculated exposure age (e.g., as discussed for sample 12030,187,C in the Group 4 section). This is due to the relatively rapid attenuation of the SCR flux (which is completely attenuated within a few cm of the lunar surface). It does not take much additional regolith cover (i.e., at conditions $<2\text{ g cm}^{-2}$) before the $^{20}\text{Ne}/^{22}\text{Ne}$ ratio does not appreciably change in comparison to the shielding depth. At this point, the uncertainties associated with the shielding tie-line allow a wide range of depths to apply to the second (i.e., “deep”) shielding depth. As a result, the range of plausible CRE ages calculable for that sample greatly increases.

In samples that have long exposure durations at depths where production rates are low, a relatively small change in the calculated “deep” shielding depth can result in a considerable change in calculated CRE age. Additionally, the range of shielding depths encompassed by the same isotopic ratio uncertainties (i.e., the $^{20}\text{Ne}/^{22}\text{Ne}$ and $^{21}\text{Ne}/^{22}\text{Ne}$ ratios) increases with increasing shielding depth due to the decrease in the difference between the modeled isotope ratios for each depth.

We, therefore, acknowledge the limitations this assumption enforces. In this respect, the model is not robust to changes in the “shallow” stage shielding conditions.

Resolving Two Stages of Exposure

One limitation of this method is found in the ratio between the shallow shielding duration to the deep shielding duration. Figure 7 demonstrates how smaller

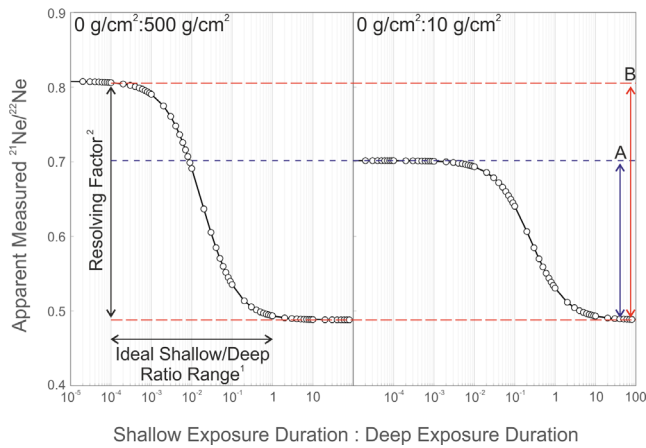


Fig. 7. Theoretical model characterizing the effects of the relative ratio of shallow and deep burial depth. This model details how a sample with a deep burial duration in excess of a factor of 100 greater than the shallow burial duration would appear to have no surface exposure according to the discussed two-stage exposure model. Shallow exposure durations in excess of the duration the sample experienced deep shielding conditions will, similarly, result in no apparent deep shielding duration within this model. (Color figure can be viewed at wileyonlinelibrary.com.)

shielding depth changes make it harder to resolve the two stages of exposure from each other. It is easier to resolve the two stages from each other in Fig. 7, scenario “B” (where the ratio changes from ~ 0.8 to 0.5 over a range of $0\text{--}500\text{ g cm}^{-2}$) than it is in scenario “A” (where the ratio changes from ~ 0.7 to 0.5 over a range of $0\text{--}10\text{ g cm}^{-2}$) due to the greater difference in the modeled $^{21}\text{Ne}/^{22}\text{Ne}$ ratio. Of greater significance is the ratio between the two shielding stage durations. Based on the model presented in Fig. 7, “deep” shielding durations between $\times 10$ and $\times 10^3$ the value of the “shallow” shielding duration are ideal for application to our modeling method because the apparent cosmogenic endmember composition can be unambiguously differentiated from the calculated shallow/deep shielding endmember compositions (shown in Fig. 7 as the ideal shallow/deep ratio range). An order of magnitude above or below that range renders the apparent cosmogenic composition change unresolvable. Samples with equal exposure durations would appear to have no “deep shielding” exposure duration. Similarly, a “deep shielding” exposure duration that is $\times 10^3$ to $\times 10^4$ longer than the “shallow shielding” exposure duration would appear to have no “shallow shielding” exposure duration (i.e., the sample would appear to have a single-stage exposure at a deep shielding depth). We, therefore, deduce that any sample with no measurable “shallow shielding” exposure duration has been on the surface for a maximum duration of $\times 10^{-3}$ of the “deep shielding” exposure duration calculated for that sample.

Geological Evolution of the Apollo 12 Landing Site

The CRE age of our sample data (Tables 4 and 5), coupled with the existing exposure age data from the Apollo 12 landing site (Fig. 8; based on data collated by Curran et al., 2020), can be used to better understand the local geological evolution of the region.

Formation of the lava flows: The Apollo 12 mare basalt lava flows (i.e., olivine, ilmenite, and pigeonite suites) were erupted between 3.129 ± 0.01 and 3.187 ± 0.006 Ga, with the additional feldspathic basalt unit forming earlier at 3.242 ± 0.013 Ga (Snape et al., 2018). It is likely these lava flows were erupted onto the surface and quickly buried, possibly by further erupted material, given the relatively short period (~ 60 Myr) over which this large quantity of basalt is thought to have crystallized (Snape et al., 2018; see also Iqbal et al., 2020). Our new exposure age data (Tables 4 and 5) show that no samples have CRE durations that match these crystallization ages. This implies that either our sample set has not resided at a depth penetrable by the cosmic ray flux for their entire existence or, at some point in their history, the samples were “reset” (i.e., a portion of some accumulated gas species within the sample were released). We note that complete degassing of a sample without causing melting of mineral phases is unlikely and the general agreement between our calculated ^{21}Ne and ^{38}Ar CRE ages suggests that severe shock-related degassing can be ruled out in all but one sample. Thus, these samples have likely spent much of their existence at depths greater than those to which the cosmic ray flux can penetrate. The compositionally distinct Apollo 12 basaltic fragments in this study likely originated from at least three different lava flows (volcanic eruptions), yet appear nonetheless to record consistent CRE ages.

It is possible that multiple stages of “deep shielding” exposure can be invoked to explain the data. For example, if a sample were to be buried very deeply for a period (i.e., $>500\text{ g cm}^{-2}$, where the production of cosmogenic isotopes can correspond to a few percent of the amount expected in an unshielded, 0 g cm^{-2} , sample), then excavated to a shallower, but still “deep” depth (e.g., $10<$ to $<500\text{ g cm}^{-2}$) for a period, the cosmogenic endmember would appear to migrate along the theoretical production rate curve before it reached an endmember composition associated with a “surface” residence. This would not be apparent in a two-stage CRE model because the resultant apparent “deep shielding” exposure stage of the sample represents an integration of the shielding conditions of all the stages of shielding below $\sim 10\text{ g cm}^{-2}$. Thus, the “deep” shielding burial depth calculated for each sample in this study likely does not represent the deepest point the

sample has ever been buried to. We note that most named craters found in the Apollo 12 landing site (and a few unnamed craters) are 3 m or greater in depth; excavation by an impact forming a crater 3 m deep is estimated to correspond to the exhumation of material from shielding depths up to 600 g cm^{-2} (Burnett et al., 1975).

Post-mare impact cratering: Next, the region was likely affected by emplacement of Eratosthenian and Copernican aged impact craters (Hubbard et al., 1971; Lindsay, 1971) such as Copernicus, located 406 km to the north; Reinhold, 196 km north; and Lansberg, 108 km to the NW (Korotev et al., 2000; Wasson & Baedeker, 1972) (see Fig. 2). Sample 12030,187 has an exposure age range (Table 4; Fig. 5) that encompasses the currently held formation age of the Copernicus crater (800 Ma, Barra et al., 2006; Eberhardt et al., 1973; Korotev et al., 2011). If the Copernicus impact event were the cause of bringing sample 12030,187 to the lunar surface, then that would imply that the sample has been under relatively shallow shielding conditions since that time. This hypothesis is based on the low average shielding depth calculated for the sample ($0\text{--}5 \text{ g cm}^{-2}$) as well as the exposure age being consistent with that of Copernicus. This shallow shielding is consistent with the enrichment of the solar wind gases component observed within this sample. However, given the chemical affinity of the sample to other Apollo 12 basalts (Alexander et al., 2016), it is more likely that ballistic projectiles released by the primary Copernicus impact event landed in the regolith near the Apollo 12 landing site and exhumed this sample from a local lava flow.

Post-Copernicus ejecta emplacement: The Apollo 12 region was later influenced by the formation of numerous small ($<1 \text{ km}$ diameter) craters (Fig. 8), continuing micrometeorite bombardment, and regolith development. These craters did not completely resurface the Apollo 12 site as Copernican ejecta rays still crosscut the area (Levine et al., 2005). Middle Crescent crater is the oldest small crater in the region (inferred by it having the most eroded crater rim). The crater has no reported age, although it is possible that the $\sim 300 \text{ Myr}$ peak in Apollo 12 sample (literature) CRE ages represents the formation of this crater. This is followed by Surveyor crater ($\sim 180\text{--}240 \text{ Myr}$), Head crater ($\sim 144 \text{ Myr}$), and Bench crater ($\sim 90 \text{ Myr}$) (Funkhouser, 1971; Wänke et al., 1971) (Fig. 8). All three of these craters still preserve ejected boulders, and Surveyor crater, the largest of the three craters, appears to penetrate most of the thickness of the upper regolith layer (Lindsay, 1971). It is, therefore, likely that at least the Surveyor crater impact excavated material from the underlying mare basalt bedrock and also KREEP-rich

Copernican fossil regolith (Korotev et al., 2011). The youngest small ($<20 \text{ m}$) craters have very fresh rims (Sharp, Halo, Block, unnamed on rim of Surveyor, Triplet: Fig. 8) and are currently thought to be $<10 \text{ Myr}$ old (Kereszturi & Steinmann, 2017). Shoemaker et al. (1970) suggest that even a small $\sim 3 \text{ m}$ crater could have excavated material from almost a complete column of the regolith cover at the Apollo 12 landing site, although it is noted that there is contention surrounding the amount of material that is redistributed by any given impact (e.g., Levine et al., 2005; Melosh, 1989).

These craters are all possible contenders for the excavation of the basalt samples with the shortest exposure ages in our study, and for producing some of the distinctive exposure age cumulative “peaks” that occur in the other Apollo 12 sample literature data (Figs. 5 and 8).

Sample 12003,316,A also has a calculated CRE age (^{21}Ne age: $467 \pm 47 \text{ Myr}$; ^{38}Ar age: $550 \pm 56 \text{ Myr}$) greater than any currently accepted local impact crater formation age. It is possible that the literature Apollo 12 sample exposure age data peak at $\sim 300 \text{ Myr}$ is related to the formation of Middle Crescent crater as these samples were collected on that crater’s ejecta blanket (although that remains purely conjecture) (Fig. 8). Nevertheless, the CRE ages calculated for 12003,316 and 12030,187 in this study are significantly older than almost all calculated exposure ages for the Apollo 12 landing site. The scarcity of samples of these ages could imply that the samples are not local to the area; however, the sample chemistry data would imply they are derived from lava flows that are at least closely related to those underlying the regolith blanket of the landing site (Alexander et al., 2014; Snape et al., 2018).

Regolith gardening: An individual soil sample may preserve the records of multiple regolith mixing events from primary and secondary crater formation, when grains or rocks are removed from depth and redeposited near the surface (Costello et al., 2018; Gault et al., 1974). Additionally, the continual breakdown of individual rock or mineral particles is greater near the lunar surface due to micrometeorite bombardment (Grün et al., 1985; Morrison & Clanton, 1979; Morrison & Zinner, 1977).

Individual fragments from soil sample 12003 yield a range of ages from $124 \pm 11 \text{ Myr}$, $188 \pm 15 \text{ Myr}$, and a group with an undefined age (and plausibly an additional fourth group between 467 ± 47 and $1138 \pm 114 \text{ Myr}$). We note that a relatively small change in depth from the surface (i.e., $<5 \text{ g cm}^{-2}$ difference) will drastically change the ability for this model to predict total cosmic ray duration ages for what we are terming the “surface exposure.” This can

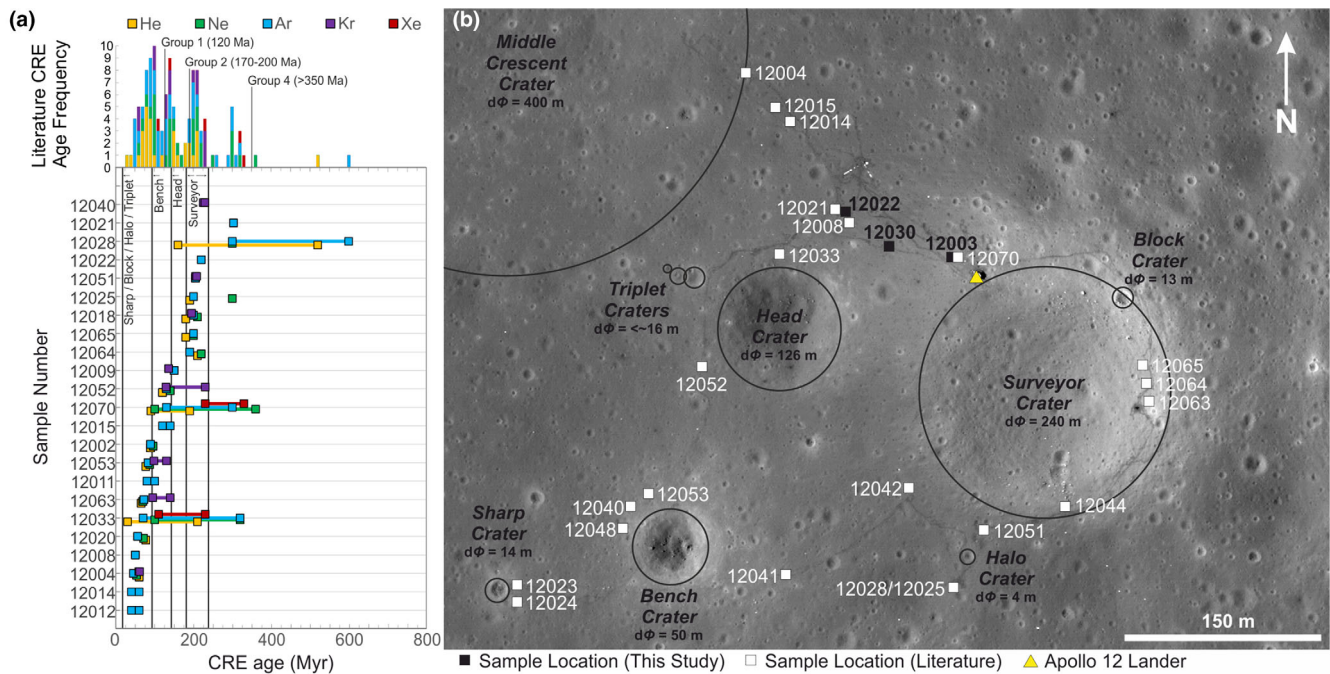


Fig. 8. a) The range of cosmic ray exposure ages reported for each sample in the literature. b) A map showing the known (or estimated) collection selenography for samples detailed in (a). These were collated using the database compiled by Curran et al. (2020) (inclusive of references: [a] Bogard et al., 1971; [b] Eugster et al., 1984; [c] Funkhouser, 1971; [d] Füre et al., 2015; [e] Hintenberger et al., 1971; [f] Marti & Lugmair, 1971; [g] Mortimer et al., 2015). Image credit: NASA Goddard Space Flight Center/ASU. (Color figure can be viewed at wileyonlinelibrary.com.)

be seen in Fig. 4b, in terms of how drawing a tie-line between 1 and 2 g cm⁻² would cause movement largely along the y axis (²¹Ne/²²Ne ratio change). Such a change in the “surface” depth would allow the “deep” depth a much wider range for this model and would therefore yield much longer surface exposure durations. However, the lack of any ²⁰Ne/²²Ne deviation away from the theoretical curve does limit the viability of this possibility. Thus, under the assumptions of our model, these samples have not resided for appreciable durations of time on the very surface of the regolith. We, therefore, infer four distinct events (or shared histories) from the samples measured. This shows that grains from within an individual soil sample do not necessarily correlate to formation or emplacement from any one single impact event but rather are likely to represent mixing together of material ejected from differing impact events. Exposure ages of Apollo bulk aliquots of soil samples (e.g., see the data plotted as ranges in Fig. 8a) may lead to a blurring of the timeline for individual events due to the wide range of ages represented in differing proportions.

Crystalline basalt boulder erosion versus local impact gardening: The observed low surface exposure ages may also be explained as a sampling relic. There will necessarily be a lifespan, or expected survival time for basalt grains of the size specified within this study.

It is possible that these findings show that basalt grains of ~2 mm size do not survive well on the lunar surface; thus, these samples were collected during their rise through the final few cm of the regolith blanket (i.e., before they had been exposed on the very surface). It is also possible that these samples were recently fragmented from larger samples, resulting in an apparent shielding depth change. Although many studies have assessed the survival times of boulders on the lunar surface (e.g., Basilevsky et al., 2013; Hörz et al., 2020; Ruesch et al., 2020), studies assessing the survival times of fine-grained regolith are scarce. Using the information available, it is not possible to discern whether any of our samples were derived from recent fragmentation of a boulder. However, two factors lead us to believe that the size of the grains within our sample set has not significantly changed for their entire CRE history. (i) The presence of solar wind composition gases within all of these basalt grain samples implies that these samples were likely exposed in their current form on the lunar surface for a period of time before collection; it is less likely that they could be a fragment of an exposed boulder surface based on (ii) barring sample 12003,310_1A; these samples do not show evidence of significant Ne gas loss (which would be expected if a boulder-disrupting impact had formed these samples). Ultimately, recent fragmentation from a

larger more shielded sample is a difficult scenario to accept for the samples measured in this study.

Implications for regolith turnover models: Our calculations suggest clusters of samples with shared or comparable histories. Given the mechanics of impact gardening, this is not overly surprising. One might expect each impact to overturn the regolith as a layer, resulting in a relatively shared history. Therefore, sampling a small area (i.e., a single soil scoop sample), it is likely that multiple grains will have progressed through the regolith at the same rate. The reality behind the history of these samples is almost certainly more complicated than this two-stage exposure modeling method allows for. There is no clear way of assessing the way in which the sample moves/moved within the “deep” shielding portion of its exposure.

Implanted Solar Wind Implications

Our gas deconvolution method allows the calculation of the “trapped” gas composition (Table S3). This component represents solar wind that has undergone mass-dependent fractionation during implantation, and subsequently lost variable amounts of the surface sited gases due to sputtering of the grain surface (Grimberg et al., 2006). We term the theoretical endmember of this composition SAIF-SW. To be in keeping with the findings of Grimberg et al. (2006, 2008), our measurements should show progressively more fractionated “trapped” component compositions with increasing surface exposure duration. However, our data do not follow this trend. Characteristics including mineralogy may affect the degree of solar wind implantation and sputtering (Burgess & Stroud, 2018), and it is possible that variable contributions of these characteristics explain our results. Additionally, the sample preparation techniques used in this study (we have worked with chips that have been split, thus, have divided their original exterior surface) do not allow for robust interrogation of the preserved solar wind concentration characteristics of these samples.

Our calculated shallow shielding ages range from (at least) 6 or 7 ± 2 Myr (Table 5). We note that this range is the lower limit of this duration due to the limitations of this model in accounting for all $0\text{--}5$ g cm⁻² shielding as exposure at 0 g cm⁻². This lies within the limits of the no shielding (0 g cm⁻²) exposure duration values calculated by Bhandari et al. (1971) of $1.3\text{--}2.6$ Myr, and the subdecimeter exposure duration of <35 Myr. We, therefore, interpret the disagreement between our calculated surface exposure durations and measured “trapped” Ne isotopic compositions as an indication that our 0 g cm⁻² assumption is an oversimplification of the shallow CRE indicator. It is likely that the values indicated by the shallow exposure

durations include a period of nonzero shielding exposure. In addition, these ages are short. This is in keeping with current theories about the emplacement of fresh ejecta onto the lunar surface by the nearby relatively recent small impacts, like Sharp crater (<10 Myr; Levine et al., 2005) (Fig. 8). This does not prevent the samples originating from an impact event of a similarly young crater that is situated closer to the sampling location (Fig. 8). Given the arguments of Wasson and Baedeker (1972), it seems likely that our samples represent a mixing between ejecta from Middle Crescent crater, Surveyor crater, and Head crater. Given these impacts are thought to be bedrock penetrating (Stöffler & Ryder, 2001), they likely introduced fresh material into the already present regolith, represented in our sample set.

Our findings support the theory that small impacts (primary and secondary) cause relatively rapid churning of the surface regolith layer (~ 1 cm reworked to homogenization within 100,000 yr: Costello et al., 2018). Our findings conform to this model and suggest that ~ 5 cm depth of regolith is more rapidly churned within the ~ 10 Myr (between the formation of the most recent named impact craters; e.g., Sharp crater, Halo crater, Triplet crater[s]) than has so far been considered. We surmise this based on the relatively short surface exposure ages (in conjunction with the findings of Bhandari et al., 1971). In addition, Fig. 7 allows us to infer that these samples had surface residency times of between $\sim 100,000$ and $\sim 300,000$ yr.

Implications for Future Exploration Missions

There is currently renewed interest in lunar exploration. Many of these interests involve understanding the volatile budget of the regolith. The findings of this study are valuable for these planned exploration missions, particularly with respect to planning in situ volatile analysis schemes. Our data show that step heating provides the ability to calculate sample-specific endmember compositions that are otherwise ambiguous (i.e., assumed based on literature average values of these endmember components) if the specific sample aliquot chemistry is well known. We note, however, that available gas extraction systems for in situ analyses are limited by their peak temperatures (e.g., the ProSPA package has a maximum temperature of 1000 °C; Barber et al., 2018). This ultimately could hamper the effectiveness of the described gas deconvolution techniques discussed in this study (see also Curran et al., 2020), and how easily applicable they are to in situ volatile analysis. This is a particular problem for Ar analyses, where clearly resolved stepped heating releases are necessary for many data

interrogation methods. The techniques described within this study are advantaged by their use of Ne, due to the lower heating temperatures required to extract the entire Ne inventory from a given sample. However, the effects of grain size on the gas release profile of a sample have yet to be extensively studied, and thus, it remains to be seen whether smaller grain size fractions would facilitate complete extraction profiles at lower total temperatures that could be implemented by currently available in situ gas extraction systems. In addition, we note that in situ major element chemistry analysis of a sample followed by destructive analysis (for volatile species measurement) is a complex process. This would potentially hinder the in situ use of this specific technique of discerning CRE histories.

Analyses of individual small grains from the lunar regolith have been shown to be of value to our understanding of the regolith evolution at a specified site (e.g., Fűri et al., 2018; Palma et al., 2002; Pepin et al., 1999; Pėron et al., 2017). This is not surprising, given each grain of lunar regolith could be expected to have a relatively unique regolith processing history. These histories would, therefore, become convoluted in a bulk analysis, where varying characteristics (such as CRE histories) would form a range of calculated CRE ages based on the proportion of each shared history represented in the bulk sample.

Currently, accurate and detailed analyses of individual regolith grains (such as those measured in this study) can only realistically be carried out by samples returned from the Moon to be analyzed back on Earth in our laboratories. Therefore, until available in situ gas release mechanisms rival the precision and control granted by laboratory-based mechanisms, sample return missions will remain invaluable to the continued development of our understanding of lunar regolith evolution (and other regolith-covered bodies).

We also note that future sampling of palaeoregolith deposits that are datable independently of their CRE (e.g., because they have been trapped between lava flows of known ages) has the potential to yield information on temporal variations in the cosmic ray flux that would be of great astrophysical interest (see discussion by Crawford et al., 2021, and references cited therein).

CONCLUSIONS

We have demonstrated a novel Ne isotopic component deconvolution method that allows the reconstruction of CRE histories that are independent of any endmember composition assumptions and of greater detail than is possible using conventional methods. We developed this method to aid the explanation of the disparity between apparent sample

shielding depths (i.e., those derived from Ne isotope analysis or Xe isotope analysis) and the known sample collection depths. We have applied this method to a selection of individual basalt chip samples from Apollo 12 lunar regolith soils and successfully derived CRE histories for all barring two of the samples analyzed.

We found that almost all samples had relatively short surface residency times based on CRE calculations (three samples showing surface exposure of 6 or 7 ± 2 Myr, the remaining samples showing surface exposure of less than a few hundred thousand years). We inferred that these samples had significantly longer residency within 500 g cm^{-2} of the lunar surface and it was during this residency that the majority of their cosmogenic noble gas fractions were produced. Our data can be explained by these basalt fragments having been crystallized (at around ~ 3.129 to 3.242 Ga: Snape et al., 2018) and buried rapidly either by a developing regolith blanket or further basalt eruptions, spending a significant portion of their history beyond the reach of cosmic rays. These basalts were then likely excavated by two (or more) small-scale impacts (e.g., the Surveyor, Bench, and Head crater formation impacts) that exhumed these samples to between 5 and 500 g cm^{-2} in two broadly identifiable groups at 124 ± 11 Myr or 188 ± 15 Myr ago. When the samples reached these depths in the regolith column, they were exposed to cosmic rays and began to accumulate cosmogenic nuclides. These samples were then, more recently, exhumed to within the top 10 cm of the regolith (likely by crater formation events such as Sharp crater) between ~ 35 Myr (Bhandari et al., 1971) and 6 ± 2 to 7 ± 2 Myr (our calculations). Additional very small impacts have further mixed the samples at the surface within the last 3 Myr.

Three of the analyzed samples do not fit these trends. Sample 12030,187 was exposed to the cosmic ray flux for significantly longer than the other measured samples. We infer that this sample may have originated from ballistic sedimentation of the local Apollo 12 lava flows by the Copernicus crater formation impact, and has likely resided in the upper few centimeters of the lunar regolith for its entire history. Two other samples (12003,314 and 12003,317) were either buried beyond 500 g cm^{-2} and very recently exhumed onto the lunar surface, or alternatively there was significant heterogeneity in terms of mineral composition between the aliquots used for chemistry analysis, and those used for noble gas analysis.

The short surface residency duration for almost all samples suggests rapid gardening of the top ~ 10 cm of the lunar regolith. These findings appear to agree with the recent revisions to the canonical regolith mixing model, proposed by Costello et al. (2018).

We find that the fragments of comparable type and texture from a single lunar regolith soil sample show distinct histories, but those histories display some degree of clustering. Thus, in a given $5 \times 5 \times 5$ cm cube of lunar regolith, many CRE histories may be represented, but the statistics of that sample are likely dominated by the larger impacts that have emplaced regolith into the sampling volume. Clusters of CRE ages suggest major overturn events (large impacts) are more significant to the Apollo 12 regolith evolution history than gradual gardening depth change, in line with the findings of Arrhenius et al. (1971).

The analysis of individual grains within the lunar regolith, even from a relatively small (i.e., few tens of cm) lunar regolith sampling area (such as that which a robotic mission may be able to access), can provide valuable information about a potentially wide region that would otherwise be unattainable for a single lunar space mission. It is the view of this study that analysis of a greater range and quantity of lunar regolith grains may further enhance our understanding of the processes and major events that have shaped the lunar surface. It would be of significant benefit to the community to analyze lunar regolith core samples in this fashion, without disturbing the fine detail stratigraphy potentially preserved therein.

Acknowledgments—We thank the NASA Apollo Curatorial staff for hosting IAC and KHJ to select the samples used for this project and to the Apollo 12 astronauts for collecting the materials used. We thank Dr Joshua Snape for his help with the Apollo 12 soils project. MCN, LA, IAC, and KHJ thank the Leverhulme Trust for financial support (RPG-2015-020 and RPG-2019-222). KHJ acknowledges funding from Royal Society grants RS/UF140190 and URF\R\201009, and KHJ and JDG acknowledge STFC grants ST/R000751/1 and ST/V000675/1. We thank E. Füre and an anonymous reviewer for their constructive comments, and I. Leya for Associate Editorial handling.

Data Availability Statement—The data that support the findings of this study are available in the supplementary material of this article.

Editorial Handling: Prof. Ingo Leya

REFERENCES

- Airapetian, V. S., Glocer, A., Gronoff, G., Hébrard, E., and Danchi, W. 2016. Prebiotic Chemistry and Atmospheric Warming of Early Earth by an Active Young Sun. *Nature Geoscience* 9: 452–5. <https://doi.org/10.1038/ngeo2719>.
- Alexander, E. C., Bates, A., Coscio, M. R., Dragon, J. C., Murthy, V. R., Pepin, R. O., and Venkatesan, T. R. 1976. K/Ar Dating of Lunar Soils II. Proceedings, 7th Lunar Science Conference, 625–48.
- Alexander, L. 2015. A Geochemical and Mineralogical Study of Lunar Basaltic Fines Collected at the Apollo 12 Landing Site. PhD thesis, Birkbeck College, University of London.
- Alexander, L., Snape, J. F., Crawford, I. A., Joy, K. H., and Downes, H. 2014. Searching for Nonlocal Lithologies in the Apollo 12 Regolith: A Geochemical and Petrological Study of Basaltic Coarse Fines from the Apollo Lunar Soil Sample 12023,155. *Meteoritics & Planetary Science* 49: 1288–304. <https://doi.org/10.1111/maps.12319>.
- Alexander, L., Snape, J. F., Joy, K. H., Downes, H., and Crawford, I. A. 2016. An Analysis of Apollo Lunar Soil Samples 12070,889, 12030,187, and 12070,891: Basaltic Diversity at the Apollo 12 Landing Site and Implications for Classification of Small-Sized Lunar Samples. *Meteoritics & Planetary Science* 51: 1654–77. <https://doi.org/10.1111/maps.12689>.
- Allton, J. H. 1989. Catalog of Apollo Lunar Surface Geological Sampling Tools and Containers Report No. JSC-23454, 1–101. Houston.
- Arrhenius, G., Liang, S., MacDougall, D., Wilkening, L., Bhandari, N., Bhat, S. et al. 1971. The Exposure History of the Apollo 12 Regolith. Proceedings, 2nd Lunar Science Conference, 2583–98.
- Arvidson, R., Drozd, R. J., Hohenberg, C. M., Morgan, C. J., and Poupeau, G. 1975. Horizontal Transport of the Regolith, Modification of Features, and Erosion Rates on the Lunar Surface. *The Moon* 13: 67–79. <https://doi.org/10.1007/BF00567508>.
- Atri, D., and Melott, A. L. 2014. Cosmic Rays and Terrestrial Life: A Brief Review. *Astroparticle Physics* 53: 186–90. <https://doi.org/10.1016/j.astropartphys.2013.03.001>.
- Barber, S. J., Wright, I. P., Abernethy, F., Anand, M., Dewar, K. R., Hodges, M., Landsberg, P. et al. 2018. ProSPA: Analysis of Lunar Polar Volatiles and ISRU Demonstration on the Moon (Abstract #2172). 49th Lunar and Planetary Science Conference. CD-ROM.
- Barra, F., Swindle, T. D., Korotev, R. L., Jolliff, B. L., Zeigler, R. A., and Olson, E. 2006. $^{40}\text{Ar}/^{39}\text{Ar}$ Dating of Apollo 12 Regolith: Implications for the Age of Copernicus and the Source of Nonmare Materials. *Geochimica et Cosmochimica Acta* 70: 6016–31. <https://doi.org/10.1016/j.gca.2006.09.013>.
- Basilevsky, A. T., Head, J. W., and Horz, F. 2013. Survival Times of Meter-Sized Boulders on the Surface of the Moon. *Planetary and Space Science* 89: 118–26. <https://doi.org/10.1016/j.pss.2013.07.011>.
- Bhandari, N., Bhat, S., Lal, D., Rajagopalan, G., Tamhane, A. S., and Venkatavaradan, V. S. 1971. High Resolution Time Averaged (Millions of Years) Energy Spectrum and Chemical Composition of Iron-Group Cosmic Ray Nuclei at 1 A. U. Based on Fossil Tracks in Apollo Samples. Proceedings, 2nd Lunar Science Conference. p. 2611.
- Bhandari, N., Goswami, J. N., Lal, D., Macdougall, D., and Tamhane, A. S. 1972. A Study of the Vestigial Records of Cosmic Rays in Lunar Rocks Using a Thick Section Technique. *Proceedings of the Indian Academy of Sciences—Section A* 76: 27–50. <https://doi.org/10.1007/BF03048334>.
- Bhandari, N., and Padia, J. T. 1974. Secular Variations in the Abundances of Heavy Nuclei in Cosmic Rays. *Science* 185: 1043–5. <https://doi.org/10.1126/science.185.4156.1043>.

- Bickel, V. T., Aaron, J., Manconi, A., Loew, S., and Mall, U. 2020. Impacts Drive Lunar Rockfalls over Billions of Years. *Nature Communications* 11: 2862. <https://doi.org/10.1038/s41467-020-16653-3>.
- Bogard, D. D., Funkhouser, J. G., Schaeffer, O. A., and Zahringer, J. 1971. Noble Gas Abundances in Lunar Material, Cosmic-Ray Spallation Products and Radiation Ages from the Sea of Tranquility and the Ocean of Storms. *Journal of Geophysical Research* 76: 2757–79. <https://doi.org/10.1029/jb076i011p02757>.
- Brett, R., Butler, P. Jr, Meyer, C. Jr, Reid, A. M., Takeda, H., and Williams, R. 1971. Apollo 12 Igneous rocks 12004, 12008, 12009, and 12022: A Mineralogical and Petrological Study. Proceedings, 2nd Lunar Science Conference, 301–17.
- Burgess, K. D., and Stroud, R. M. 2018. Phase-Dependent Space Weathering Effects and Spectroscopic Identification of Retained Helium in a Lunar Soil Grain. *Geochimica et Cosmochimica Acta* 224: 64–79. <https://doi.org/10.1016/j.gca.2017.12.023>.
- Burnett, D. S., Drozd, R. J., Morgan, C. J., and Podosek, F. A. 1975. Exposure History of Bench Crater rocks. Proceedings, 6th Lunar Science Conference, pp. 2219–40.
- Butler, P. 1972. Compositional Characteristics of Olivines from Apollo 12 Samples. *Geochimica et Cosmochimica Acta* 36: 773–85. [https://doi.org/10.1016/0016-7037\(72\)90087-7](https://doi.org/10.1016/0016-7037(72)90087-7).
- Calio, A. J., Stephenson, W. K., Simmons, G., Wade, L. C., Bean, A. L., Conrad, C. Jr, Gordon, R. et al. 1970. Apollo 12 Preliminary Science Report (NASA SP-235).
- Cameron, E. N. 1971. Opaque Minerals in Certain Lunar Rocks from Apollo 12. Proceedings, 2nd Lunar Science Conference, 193–206.
- Codilean, A. T., Bishop, P., Stuart, F. M., Hoey, T. B., Fabel, D., and Freeman, S. P. H. T. 2008. Single-Grain Cosmogenic ²¹Ne Concentrations in Fluvial Sediments Reveal Spatially Variable Erosion Rates. *Geology* 36: 159–62. <https://doi.org/10.1130/G24360A.1>.
- Cohen, O., Drake, J. J., and Kóta, J. 2012. The Cosmic-Ray Intensity Near the Archean Earth. *The Astrophysical Journal* 760: 85. <https://doi.org/10.1088/0004-637X/760/1/85>.
- Costello, E. S., Ghent, R. R., and Lucey, P. G. 2018. The Mixing of Lunar Regolith: Vital Updates to a Canonical Model. *Icarus* 314: 327–44. <https://doi.org/10.1016/j.icarus.2018.05.023>.
- Crawford, I. A., Fagents, S. A., Joy, K. H., and Rumpf, M. E. 2010. Lunar Palaeoregolith Deposits as Recorders of the Galactic Environment of the Solar System and Implications for Astrobiology. *Earth, Moon, and Planets* 107: 75–85. <https://doi.org/10.1007/s11038-010-9358-z>.
- Crawford, I. A., Joy, K. H., and Fagents, S. A. 2007. Full Moon Exploration. *Astronomy & Geophysics* 48: 3.18–21. <https://doi.org/10.1111/j.1468-4004.2007.48318.x>.
- Crawford, I. A., Joy, K., Pasckert, J. H., and Hiesinger, H. 2021. The Lunar Surface as a Recorder of Astrophysical Processes. *Philosophical Transactions of the Royal Society A* 378: 20190562.
- Curran, N. M., Nottingham, M., Alexander, L., Crawford, I. A., Füre, E., and Joy, K. H. 2020. A Database of Noble Gases in Lunar Samples in Preparation for Mass Spectrometry on the Moon. *Planetary and Space Science* 182: 104823.
- Davies, M. E., and Colvin, T. R. 2000. Lunar Coordinates in the Regions of the Apollo Landers. *Journal of Geophysical Research E: Planets* 105: 20277–80. <https://doi.org/10.1029/1999JE001165>.
- Eberhardt, P., Geiss, J., Grögler, N., and Stettler, A. 1973. How Old Is the Crater Copernicus? *The Moon* 8: 104–14. <https://doi.org/10.1007/BF00562752>.
- Erykin, A. D., and Wolfendale, A. W. 2010. Long Term Time Variability of Cosmic Rays and Possible Relevance to the Development of Life on Earth. *Surveys in Geophysics* 31: 383–98. <https://doi.org/10.1007/s10712-010-9097-8>.
- Eugster, O. 2003. Cosmic-Ray Exposure Ages of Meteorites and Lunar Rocks and Their Significance. *Geochemistry* 63: 3–30. <https://doi.org/10.1078/0009-2819-00021>.
- Eugster, O., Eberhardt, P., Geiss, J., Grögler, N., Jungck, M., Meier, F., Mörgeli, M., and Niederer, F. 1984. Cosmic Ray Exposure Histories of Apollo 14, Apollo 15, and Apollo 16 Rocks. *Journal of Geophysical Research* 89: B498–512. <https://doi.org/10.1029/JB089iS02p0B498>.
- Eugster, O., Herzog, G. F., Marti, K., and Caffee, M. W. 2006. Irradiation Records, Cosmic-Ray Exposure Ages, and Transfer Times of Meteorites. In *Meteorites and the Early Solar System II*, edited by D. S. Laurette and H. Y. McSween Jr., 829–51. Tucson, Arizona: The University of Arizona Press.
- Fagan, A. L., Joy, K. H., Bogard, D. D., and Kring, D. A. 2014. Ages of Globally Distributed Lunar Paleoregoliths and Soils from 3.9 Ga to the Present. *Earth, Moon, and Planets* 112: 59–71. <https://doi.org/10.1007/s11038-014-9437-7>.
- Fagents, S. A., Rumpf, M. E., Crawford, I. A., and Joy, K. H. 2010. Preservation Potential of Implanted Solar Wind Volatiles in Lunar Paleoregolith Deposits Buried by Lava Flows. *Icarus* 207: 595–604. <https://doi.org/10.1016/j.icarus.2009.11.033>.
- Fernandes, V., and Artemieva, N. 2012. Impact Ejecta Temperature Profile on the Moon—What Are the Effects on the Ar-Ar Dating Method? (Abstract #1367). 43rd Lunar and Planetary Science Conference. CD-ROM.
- Funkhouser, J. 1971. Noble Gas Analysis of KREEP Fragments in Lunar Soil 12033 and 12070. *Earth and Planetary Science Letters* 12: 263–72. [https://doi.org/10.1016/0012-821X\(71\)90210-X](https://doi.org/10.1016/0012-821X(71)90210-X).
- Füre, E., Barry, P. H., Taylor, L. A., and Marty, B. 2015. Indigenous Nitrogen in the Moon: Constraints from Coupled Nitrogen-Noble Gas Analyses of Mare Basalts. *Earth and Planetary Science Letters* 431: 195–205. <https://doi.org/10.1016/j.epsl.2015.09.022>.
- Füre, E., Marty, B., and Assonov, S. S. 2012. Constraints on the Flux of Meteoritic and Cometary Water on the Moon from Volatile Element (N-Ar) Analyses of Single Lunar Soil Grains, Luna 24 Core. *Icarus* 218: 220–9. <https://doi.org/10.1016/j.icarus.2011.11.037>.
- Füre, E., Zimmermann, L., Deloule, E., and Trappitsch, R. 2020. Cosmic Ray Effects on the Isotope Composition of Hydrogen and Noble Gases in Lunar Samples: Insights from Apollo 12018. *Earth and Planetary Science Letters* 550: 116550. <https://doi.org/10.1016/j.epsl.2020.116550>.
- Füre, E., Zimmermann, L., and Saal, A. E. 2018. Apollo 15 Green Glass He-Ne-Ar Signatures—In Search for Indigenous Lunar Noble Gases. *Geochemical Perspectives Letters* 8: 1–5. <https://doi.org/10.7185/geochemlet.1819>.
- Gault, E. D., Horz, F., Brownlee, E. D., and Hartung, B. J. 1974. Mixing of the Lunar Regolith. Proceedings, 5th Lunar Science Conference, pp. 2365–86.

- Gilmour, J. 2017. Extraction of Physical Quantities from Isotope Mixing Diagrams. <https://doi.org/10.17632/vhdkpg2jsk.1>.
- Globus, N., and Blandford, R. D. 2020. The Chiral Puzzle of Life. *The Astrophysical Journal Letters* 895: L11. <https://doi.org/10.3847/2041-8213/ab8dc6>.
- Greer, J., Rout, S. S., Isheim, D., Seidman, D. N., Wieler, R., and Heck, P. R. 2020. Atom Probe Tomography of Space-Weathered Lunar Ilmenite Grain Surfaces. *Meteoritics & Planetary Science* 55: 426–40. <https://doi.org/10.1111/maps.13443>.
- Grimberg, A., Baur, H., Bochsler, P., Bühler, F., Burnett, D. S., Hays, C. C., Heber, V. S., Jurewicz, A. J. G., and Wieler, R. 2006. Solar Wind Neon from Genesis: Implications for the Lunar Noble Gas Record. *Science* 314: 1133–5. <https://doi.org/10.1126/science.1133568>.
- Grimberg, A., Baur, H., Bühler, F., Bochsler, P., and Wieler, R. 2008. Solar Wind Helium, Neon, and Argon Isotopic and Elemental Composition: Data from the Metallic Glass Flown on NASA's Genesis Mission. *Geochimica et Cosmochimica Acta* 72: 626–45. <https://doi.org/10.1016/j.gca.2007.10.017>.
- Grün, E., Zook, H. A., Fechtig, H., and Giese, R. H. 1985. Collisional Balance of the Meteoritic Complex. *Icarus* 62: 244–72. [https://doi.org/10.1016/0019-1035\(85\)90121-6](https://doi.org/10.1016/0019-1035(85)90121-6).
- Györe, D., Stuart, F. M., Gilfillan, S. M. V., and Waldron, S. 2015. Tracing Injected CO₂ in the Cranfield Enhanced Oil Recovery Field (MS, USA) Using He, Ne and Ar Isotopes. *International Journal of Greenhouse Gas Control* 42: 554–61. <https://doi.org/10.1016/j.ijggc.2015.09.009>.
- Heber, V. S., Baur, H., and Wieler, R. 2003. Helium in Lunar Samples Analyzed by High-Resolution Stepwise Etching: Implications for the Temporal Constancy of Solar Wind Isotopic Composition. *The Astrophysical Journal* 597: 602–14. <https://doi.org/10.1086/378402>.
- Heiken, G. H., Vaniman, D. T., and French, B. M. 1991. *Lunar Sourcebook*. Cambridge: University of Cambridge.
- Herzog, G. F., and Caffee, M. W. 2014. Cosmic-Ray Exposure Ages of Meteorites. In *Volume 1: Meteorites and Cosmochemical Processes*, edited by H. D. Holland and K. K. Turekian. Treatise on Geochemistry, 2nd edn, 419–54. Amsterdam: Elsevier Ltd. <https://doi.org/10.1016/B978-0-08-095975-7.00110-8>.
- Hiesinger, H., Head, J. W. III, Wolf, U., Jaumann, R., and Neukum, G. 2003. Ages and Stratigraphy of Mare Basalts in Oceanus Procellarum, Mare Nubium, Mare Cognitum, and Mare Insularum. *Journal of Geophysical Research: Planets* 108: 5065. <https://doi.org/10.1029/2002je001985>.
- Hiesinger, H., Van Der Bogert, C. H., Pasckert, J. H., Funcke, L., Giacomini, L., Ostrach, L. R., and Robinson, M. S. 2012. How Old Are Young Lunar Craters? *Journal of Geophysical Research E: Planets* 117: 1–15. <https://doi.org/10.1029/2011JE003935>.
- Hintenberger, H., Weber, H. W., and Takaoka, N. 1971. Concentrations and Isotopic Abundances of the Rare Gases in Lunar Matter. Proceedings, 2nd Lunar Science Conference, 1607–25.
- Hohenberg, C. M., Marti, K., Podosek, F. A., Reedy, R., and Shrick, J. R. 1978. Comparisons Between Observed and Predicted Cosmogenic Gases in Lunar Samples. Proceedings, 9th Lunar and Planetary Science Conference, 2311–44.
- Hörz, F., Basilevsky, A. T., Head, J. W., and Cintala, M. J. 2020. Erosion of Lunar Surface Rocks by Impact Processes: A Synthesis. *Planetary and Space Science* 194: 105105. <https://doi.org/10.1016/j.pss.2020.105105>.
- Hubbard, N. J., and Gast, P. W. 1971. Chemical Composition and Origin of Nonmare Lunar Basalts. Proceedings of the 2nd Lunar Science Conference, 999–1020.
- Hubbard, N. J., Meyer, C., Gast, P. W., and Wiesmann, H. 1971. The Composition and Derivation of Apollo 12 Soils. *Earth and Planetary Science Letters* 10: 341–50. [https://doi.org/10.1016/0012-821X\(71\)90040-9](https://doi.org/10.1016/0012-821X(71)90040-9).
- Iqbal, W., Hiesinger, H., and van der Bogert, C. H. 2020. Geological Mapping and Chronology of Lunar Landing Sites: Apollo 12. *Icarus* 352: 113991. <https://doi.org/10.1016/j.icarus.2020.113991>.
- Jasinski, J. M., Nordheim, T. A., Hasegawa, Y., and Murphy, N. 2020. The Importance of Local Interstellar Conditions on the Galactic Cosmic-Ray Spectrum at Exoplanets. *The Astrophysical Journal* 899: L18. <https://doi.org/10.3847/2041-8213/aba7c8>.
- Jolliff, B. L., Gillis, J. J., Korotev, R. L., and Haskin, L. A. 2000. On the Origin of Nonmare Materials at the Apollo 12 Landing Site (Abstract #1671). 31st Lunar and Planetary Science Conference. CD-ROM.
- Joy, K. H., Crawford, I. A., Curran, N. M., Zolensky, M., Fagan, A. F., and Kring, D. A. 2016. The Moon: An Archive of Small Body Migration in the Solar System. *Earth, Moon, and Planets* 118: 133–58. <https://doi.org/10.1007/s11038-016-9495-0>.
- Joy, K. H., Kring, D. A., Bogard, D. D., McKay, D. S., and Zolensky, M. E. 2011. Re-Examination of the Formation Ages of the Apollo 16 Regolith Breccias. *Geochimica et Cosmochimica Acta* 75: 7208–25. <https://doi.org/10.1016/j.gca.2011.09.018>.
- Kereszturi, A., and Steinmann, V. 2017. Characteristics of Small Young Lunar Impact Craters Focusing on Current Production and Degradation on the Moon. *Planetary and Space Science* 148: 12–27. <https://doi.org/10.1016/j.pss.2017.09.010>.
- Korotev, R. L., Jolliff, B. L., and Zeigler, R. A. 2000. The KREEP Components of the Apollo 12 Regolith (Abstract #1363). 31st Lunar and Planetary Science Conference. CD-ROM.
- Korotev, R. L., Jolliff, B. L., Zeigler, R. A., Seddio, S. M., and Haskin, L. A. 2011. Apollo 12 Revisited. *Geochimica et Cosmochimica Acta* 75: 1540–73. <https://doi.org/10.1016/j.gca.2010.12.018>.
- Levine, J., Becker, T. A., Muller, R. A., and Renne, P. R. 2005. ⁴⁰Ar/³⁹Ar Dating of Apollo 12 Impact Spherules. *Geophysical Research Letters* 32: L15201. <https://doi.org/10.1029/2005GL022874>.
- Lewis, J. S. 2004. III. General Description of the Solar System. *International Geophysics* 87: 50–76. [https://doi.org/10.1016/S0074-6142\(04\)80017-2](https://doi.org/10.1016/S0074-6142(04)80017-2).
- Leya, I., Neumann, S., Wieler, R., and Michel, R. 2001. The Production of Cosmogenic Nuclides by Galactic Cosmic-Ray Particles for 2N Exposure Geometries. *Meteoritics & Planetary Science* 36: 1547–61. <https://doi.org/10.1111/j.1945-5100.2001.tb01845.x>.
- Li, L., and Mustard, J. F. 2005. On Lateral Mixing Efficiency of Lunar Regolith. *Journal of Geophysical Research E: Planets* 110: 1–16. <https://doi.org/10.1029/2004JE002295>.
- Li, Q.-L., Zhou, Q., Liu, Y., Xiao, Z., Lin, Y., Li, J.-H., Ma, H.-X. et al. 2021. Two-Billion-Year-Old Volcanism on the Moon from Chang'e-5 Basalts. *Nature* 600: 54–8. <https://doi.org/10.1038/s41586-021-04100-2>.

- Lindsay, J. F. 1971. Sedimentology of Apollo 11 and 12 Lunar Soils. *SEPM Journal of Sedimentary Research* 41: 780–97. <https://doi.org/10.1306/74d72356-2b21-11d7-8648000102c1865d>.
- Lorenzetti, S., Busemann, H., and Eugster, O. 2005. Regolith History of Lunar Meteorites. *Meteoritics & Planetary Science* 40: 315–27. <https://doi.org/10.1111/j.1945-5100.2005.tb00383.x>.
- Lucey, P., Korotev, R. L., Gillis, J. J., Taylor, L. A., Lawrence, D., Campbell, B. A., Elphic, R. et al. 2018. Understanding the Lunar Surface and Space-Moon Interactions. In *New Views of the Moon*, edited by B. L. Jolliff, M. A. Wieczorek, C. K. Shearer, and C. R. Neal, 83–220. Berlin: De Gruyter <https://doi.org/10.1515/9781501509537-006>.
- Manka, R. H., and Michel, F. C. 1970. Lunar Atmosphere as a Source of Argon-40 and Other Lunar Surface Elements. *Science* 169: 278–80. <https://doi.org/10.1126/science.169.3942.278>.
- Marti, K., and Lugmair, G. W. 1971. Kr81-Kr and K-Ar40 Ages, Cosmic Ray Spallation Products and Neutron Effects in Apollo 11 and 12 Lunar Samples. Proceedings, 2nd Lunar Science Conference, 62.
- Marvin, U. B. 1978. Apollo 12 Coarse Fines (2–10): Sample Locations, Descriptions, and Inventory. Report No. JSC 14434. National Aeronautics and Space Administration.
- Masarik, J., and Reedy, R. C. 1994. Effects of Bulk Composition on Nuclide Production Processes in Meteorites. *Geochimica et Cosmochimica Acta* 58: 5307–17. [https://doi.org/10.1016/0016-7037\(94\)90314-X](https://doi.org/10.1016/0016-7037(94)90314-X).
- Matsuda, J., Matsumoto, T., Sumino, H., Nagao, K., Yamamoto, J., Miura, Y., Kaneoka, I., Takahata, N., and Sano, Y. 2002. The 3He/4He Ratio of the New Internal He Standard of Japan (HESJ). *Geochemical Journal* 36: 191–5. <https://doi.org/10.2343/geochemj.36.191>.
- McKay, D. S., Bogard, D. D., Morris, R. V., Korotev, R. L., Johnson, P., and Wentworth, S. J. 1986. Apollo 16 Regolith Breccias: Characterization and Evidence for Early Formation in the Mega-Regolith. *Journal of Geophysical Research: Solid Earth* 91: 277–303. <https://doi.org/10.1029/jb091ib04p0d277>.
- McKay, D. S., Heiken, G. H., Basu, A., Blanford, G., Simon, S., Reedy, R., French, B. M., and Papike, J. J. 1991. The Lunar Regolith. In *The Lunar Sourcebook: A User's Guide to the Moon*, edited by G. H. Heiken, D. T. Vaniman, and B. M. French, 285–356. Cambridge: Cambridge University Press.
- Melosh, H. J. 1989. *Impact Cratering: A Geologic Process*. Oxford: Clarendon Press.
- Melott, A. L., Thomas, B. C., Kachelrieß, M., Semikoz, D. V., and Overholt, A. C. 2017. A Supernova at 50 pc: Effects on the Earth's Atmosphere and Biota. *The Astrophysical Journal* 840: 105. <https://doi.org/10.3847/1538-4357/aa6c57>.
- Mighani, S., Wang, H., Shuster, D. L., Borlina, C. S., Nichols, C. I. O., and Weiss, B. P. 2020. The End of the Lunar Dynamo. *Science Advances* 6: eaax0883. <https://doi.org/10.1126/sciadv.aax0883>.
- Morrison, D. A., and Clanton, U. S. 1979. Properties of Microcraters and Cosmic Dust of Less Than 1000 Å Dimensions. Proceedings, 10th Lunar and Planetary Science Conference, pp. 1649–63.
- Morrison, D. A., and Zinner, E. 1977. 12054 and 76215: New Measurements of Interplanetary Dust and Solar Flare Fluxes. Proceedings, 8th Lunar Science Conference, pp. 841–63.
- Mortimer, J., Verchovsky, A. B., Anand, M., Gilmour, I., and Pillinger, C. T. 2015. Simultaneous Analysis of Abundance and Isotopic Composition of Nitrogen, Carbon, and Noble Gases in Lunar Basalts: Insights into Interior and Surface Processes on the Moon. *Icarus* 255: 3–17. <https://doi.org/10.1016/j.icarus.2014.10.006>.
- Neal, C. R., Hacker, M. D., Snyder, G. A., Taylor, L. A., Liu, Y.-G., and Schmitt, R. A. 1994a. Basalt Generation at the Apollo 12 Site, Part 1: New Data, Classification, and Re-Evaluation. *Meteoritics* 29: 334–48. <https://doi.org/10.1111/j.1945-5100.1994.tb00597.x>.
- Neal, C. R., Hacker, M. D., Snyder, G. A., Taylor, L. A., Liu, Y.-G., and Schmitt, R. A. 1994b. Basalt Generation at the Apollo 12 Site, Part 2: Source Heterogeneity, Multiple Melts, and Crustal Contamination. *Meteoritics* 29: 349–61. <https://doi.org/10.1111/j.1945-5100.1994.tb00598.x>.
- Neal, C. R., and Taylor, L. A. 1992. Petrogenesis of Mare Basalts: A Record of Lunar Volcanism. *Geochimica et Cosmochimica Acta* 56: 2177–211. [https://doi.org/10.1016/0016-7037\(92\)90184-k](https://doi.org/10.1016/0016-7037(92)90184-k).
- Oberbeck, V. R. 1975. The Role of Ballistic Erosion and Sedimentation in Lunar Stratigraphy. *Reviews of Geophysics* 13: 337–62. <https://doi.org/10.1029/RG013i002p00337>.
- Omidi, N., Zhou, X. Y., Russell, C. T., and Angelopoulos, V. 2019. The Dominant Role of Energetic Ions in Solar Wind Interaction with the Moon. *Journal of Geophysical Research: Space Physics* 124: 3176–92. <https://doi.org/10.1029/2018JA026243>.
- Palma, R. L., Becker, R. H., Pepin, R. O., and Schlutter, D. J. 2002. Irradiation Records in Regolith Materials, II: Solar Wind and Solar Energetic Particle Components in Helium, Neon, and Argon Extracted from Single Lunar Mineral Grains and from the Kapoeta Howardite by Stepwise Pulse Heating. *Geochimica et Cosmochimica Acta* 66: 2929–58. [https://doi.org/10.1016/S0016-7037\(02\)00853-0](https://doi.org/10.1016/S0016-7037(02)00853-0).
- Pepin, R. O., Becker, R. H., and Schlutter, D. J. 1999. Irradiation Records in Regolith Materials. I: Isotopic Compositions of Solar-Wind Neon and Argon in Single Lunar Mineral Grains. *Geochimica et Cosmochimica Acta* 63: 2145–62. [https://doi.org/10.1016/S0016-7037\(99\)00002-2](https://doi.org/10.1016/S0016-7037(99)00002-2).
- Péron, S., Moreira, M., Putlitz, B., and Kurz, M. D. 2017. Solar Wind Implantation Supplied Light Volatiles During the First Stage of Earth Accretion. *Geochemical Perspectives Letters* 3: 151–9. <https://doi.org/10.7185/geochemlet.1718>.
- Poluianov, S., Kovaltsov, G. A., and Usoskin, I. G. 2018. Solar Energetic Particles and Galactic Cosmic Rays Over Millions of Years as Inferred from Data on Cosmogenic ²⁶Al in Lunar Samples. *Astronomy & Astrophysics* 618: 96. <https://doi.org/10.1051/0004-6361/201833561>.
- Poppe, A. R., Garrick-Bethell, I., and Fatemi, S. 2021. Fractionation of Solar Wind Minor Ion Precipitation by the Lunar Paleomagnetosphere. *Planetary Science Journal* 2: 60. <https://doi.org/10.3847/PSJ/abea7d>.
- Potgieter, M. S. 2013. Solar Modulation of Cosmic Rays. *Living Reviews in Solar Physics* 10: 3. <https://doi.org/10.12942/lrsp-2013-3>.
- Rao, M. N., Garrison, D. H., Bogard, D. D., and Reedy, R. C. 1994. Determination of the Flux and Energy

- Distribution of Energetic Solar Protons in the Past 2 Myr Using Lunar Rock 68815. *Geochimica et Cosmochimica Acta* 58: 4231–45. [https://doi.org/10.1016/0016-7037\(94\)90275-5](https://doi.org/10.1016/0016-7037(94)90275-5).
- Reedy, R. C., Herzog, G. F., and Jessberger, E. K. 1979. The Reaction $Mg(n, \alpha)Ne$ at 14.1 and 14.7 MeV: Cross Sections and Implications for Meteorites. *Earth and Planetary Science Letters* 44: 341–8. [https://doi.org/10.1016/0012-821X\(79\)90182-1](https://doi.org/10.1016/0012-821X(79)90182-1).
- Rhodes, J. M., Blanchard, D. P., Dungan, M. A., Brannon, J. C., and Rodgers, K. V. 1977. Chemistry of Apollo 12 Mare Basalts: Magma Types and Fractionation Processes. Proceedings, 8th Lunar Science Conference, pp. 1305–38.
- Rodgers-Lee, D., Vidotto, A. A., Taylor, A. M., Rimmer, P. B., and Downes, T. P. 2020. The Galactic Cosmic Ray Intensity at the Evolving Earth and Young Exoplanets. *Monthly Notices of the Royal Astronomical Society* 499: 2124–37. <https://doi.org/10.1093/mnras/staa2737>.
- Ruesch, O., Sefton-Nash, E., Vago, J. L., Küppers, M., Pasckert, J. H., Krohn, K., and Otto, K. 2020. In Situ Fragmentation of Lunar Blocks and Implications for Impacts and Solar-Induced Thermal Stresses. *Icarus* 336: 113431. <https://doi.org/10.1016/j.icarus.2019.113431>.
- Sapundjiev, D., Verhulst, T., and Stankov, S. 2020. International Database of Neutron Monitor Measurements: Development and Applications. In *Knowledge Discovery in Big Data from Astronomy and Earth Observation*, edited by P. Škoda and F. Adam, 371–83. Amsterdam: Elsevier. <https://doi.org/10.1016/B978-0-12-819154-5.00032-1>.
- Saxena, P., Killen, R. M., Airapetian, V., Petro, N. E., Curran, N. M., and Mandell, A. M. 2019. Was the Sun a Slow Rotator? Sodium and Potassium Constraints from the Lunar Regolith. *The Astrophysical Journal* 876: L16. <https://doi.org/10.3847/2041-8213/ab18fb>.
- Shaviv, N. J. 2006. Long-Term Variations in the Galactic Environment of the Sun. In *Solar Journey: The Significance of Our Galactic Environment for the Heliosphere and Earth*, edited by P. C. Frisch, 99–131. Dordrecht: Springer. https://doi.org/10.1007/1-4020-4557-3_5.
- Shoemaker, E. M., Batson, R. M., Bean, A. L., Conrad, C. Jr, Dahlem, D. H., Goddard, E. N., Hait, M. H. et al. 1970. *Preliminary Geological Investigation of the Apollo 12 Landing Site, Part A. Apollo 12 Preliminary Science Report*. Washington, D.C.: NASA Office of Technology Utilization.
- Smith, T., Cook, D. L., Merchel, S., Pavetich, S., Rugel, G., Scharf, A., and Leya, I. 2019. The Constancy of Galactic Cosmic Rays as Recorded by Cosmogenic Nuclides in Iron Meteorites. *Meteoritics & Planetary Science* 54: 2951–76. <https://doi.org/10.1111/maps.13417>.
- Snape, J. F., Davids, B., Nemchin, A. A., Whitehouse, M. J., and Bellucci, J. J. 2018. Constraining the Timing and Sources of Volcanism at the Apollo 12 Landing Site Using New Pb Isotopic Compositions and Crystallisation Ages. *Chemical Geology* 482: 101–12. <https://doi.org/10.1016/j.chemgeo.2018.02.009>.
- Snape, J. F., Joy, K. H., Crawford, I. A., and Alexander, L. Sample 12003. *Meteoritics & Planetary Science* 49: 842–71. <https://doi.org/10.1111/maps.12285>.
- Spray, J. G. 2016. Lithification Mechanisms for Planetary Regoliths: The Glue that Binds. *Annual Review of Earth and Planetary Sciences* 44: 139–74. <https://doi.org/10.1146/annurev-earth-060115-012203>.
- Spudis, P. D. 1996. *The Once and Future Moon*. Washington, D.C.: Smithsonian Institution Press.
- Spudis, P. D., Hawke, B. R., and Lucey, P. G. 1988. Materials and Formation of the Imbrium Basin. 18th Lunar and Planetary Science Conference, 155–68.
- Stöffler, D., and Ryder, G. 2001. Stratigraphy and Isotope Ages of Lunar Geologic Units: Chronological Standard for the Inner Solar System. *Space Science Reviews* 96: 9–54. <https://doi.org/10.1023/A:1011937020193>.
- Thiemens, M. H., and Clayton, R. N. 1980. Ancient Solar Wind in Lunar Microbreccias. *Earth and Planetary Science Letters* 47: 34–42. [https://doi.org/10.1016/0012-821X\(80\)90101-6](https://doi.org/10.1016/0012-821X(80)90101-6).
- Todd, P. 1994. Cosmic Radiation and Evolution of Life on Earth: Roles of Environment, Adaptation and Selection. *Advances in Space Research* 14: 305–13. [https://doi.org/10.1016/0273-1177\(94\)90483-9](https://doi.org/10.1016/0273-1177(94)90483-9).
- Wänke, H., Wlotzka, F., Baddenhausen, H., Balacescu, A., Spettel, B., Teschke, F., Jagoutz, E., Kruse, H., Quijano-Rico, M., and Rieder, R. 1971. Apollo 12 Samples: Chemical Composition and Its Relation to Sample Locations and Exposure Ages, the Two Component Origin of the Various Soil Samples and Studies on Lunar Metallic Particles. Proceedings, 2nd Lunar Science Conference, pp. 1187–208.
- Wasson, J. T., and Baedecker, P. A. 1972. Provenance of Apollo 12 KREEP. Proceedings, 3rd Lunar Science Conference, pp. 1315–26.
- Weill, D. F., Grieve, R. A., McCallu, I. S., and Bottinga, Y. 1971. Mineralogy-Petrology of Lunar Samples. Microprobe Studies of Samples 12021 and 12022; Viscosity of Melts of Selected Lunar Compositions. Proceedings, 2nd Lunar Science Conference, 413–30.
- Wentworth, S. J., McKay, D. S., Lindstrom, D. J., Basu, A., Martinez, R. R., Bogard, D. D., and Garrison, D. H. 1994. Apollo 12 Ropy Glasses Revisited. *Meteoritics* 29: 323–33. <https://doi.org/10.1111/j.1945-5100.1994.tb00596.x>.
- Wieler, R. 2002. Noble Gases in the Solar System. *Reviews in Mineralogy and Geochemistry* 47: 21–70. <https://doi.org/10.2138/rmg.2002.47.2>.
- Wieler, R. 2016. Do Lunar and Meteoritic Archives Record Temporal Variations in the Composition of Solar Wind Noble Gases and Nitrogen? A Reassessment in the Light of Genesis Data. *Chemie Der Erde—Geochemistry* 76: 463–80. <https://doi.org/10.1016/j.chemer.2016.06.001>.
- Wieler, R., Beer, J., and Leya, I. 2013. The Galactic Cosmic Ray Intensity over the Past 10^6 – 10^9 Years as Recorded by Cosmogenic Nuclides in Meteorites and Terrestrial Samples. *Space Science Reviews* 176: 351–63. <https://doi.org/10.1007/s11214-011-9769-9>.
- Wilhelms, D. E., McCauley, J. F., and Trask, N. J. 1987. The Geologic History of the Moon. *U.S. Geological Survey Professional Paper* 1348: 302. <https://doi.org/10.3133/pp1348>.

SUPPORTING INFORMATION

Additional supporting information may be found in the online version of this article.

Table S1. Chemistry data used to calculate the theoretical cosmogenic nuclide production rate ratios for our models. These data are collated from Alexander et al. (2014, 2016), Alexander (2015), and Snape et al. (2014). Measurements were made on fragments of the same grains used for noble gas analyses within this study.

Table S2. Noble gas concentrations and isotopic ratios measured in the Apollo 12 basalt sample set. Uncertainties reported are 1σ confidence interval.

Table S3. Trapped, cosmogenic, and “deep” shielding production rate ratios used in the calculation of the two-stage cosmic ray exposure histories. Uncertainties reported are 1σ confidence interval.

Table S4. Mahalanobis fit parameters calculated for each sample’s mixing line. Uncertainties are 1σ .

Fig. S1. Flow chart detailing the procedure used to divide the measured gas into “trapped” and cosmogenic component fractions, as well as shallow and deep

shielding stage fractions. Note: the three-isotope plot axes are different to those used within the main manuscript text. Plots within the manuscript are visualized in a way that aids comparison to similar plots available in the literature.

Fig. S2. Step-wise Ar isotope data for each sample. The data is sensitivity corrected. Blank correction was unnecessary. Each plot also shows the theoretical range of possible cosmogenic components specific to each sample, these ranges are calculated using chemistry data from Snape et al. (2014) and Alexander et al. (2016) and production rate models of Hohenberg et al. (1978). Bulk sample measurement refers to the isotopic ratio representative of a summed total gas inventory for the sample.

Fig. S3. Three-isotope plot showing all measured releases from all samples, according to the release temperature. Total points refer to the summed composition released from each sample. This plot includes steps where the sample was reheated to the same temperature in order to ensure it had been totally degassed.
